UNIVERSITY OF CALIFORNIA
RIVERSIDE

Searching for the Geodetic Signature of Wastewater Injection at The Geysers Geothermal Field

A Thesis submitted in partial satisfaction
of the requirements for the degree of

Master of Science

in

Geological Sciences

by

Rachel LeeAnn Terry

March 2019

Thesis Committee:

Dr. Gareth Funning, Chairperson
Dr. Heather Ford
Dr. Nicolas Barth

The Thesis of Rachel LeeAnn Terry is approved:

Committee Chairperson

University of California, Riverside

Acknowledgments

I would like to thank my principal investigator, **Gareth Funning**, for all of his help, guidance and encouragement throughout my time here at UC-Riverside. He brought me on as a graduate student from an unconventional background and continued to maintain high expectations for me, helping me to push farther than I would have otherwise. He cares about each one of his graduate students individually and in their path beyond graduate school, whatever they may choose. **Michael Floyd** (MIT), a co-author on this work, was also a source of guidance throughout the project. Without him and Gareth installing the GPS in the Geysers field back in 2012 and 2013, I would not have been able to do this project! It has also been fun working with both of them, socializing at conferences and spending many hours together during GPS campaigns. I would also like to thank **Craig Hartline** from Calpine for answering any questions about The Geysers geothermal field. He was willing to help or provide data at any point during the project.

Thanks to **Heather Ford** and **Nicolas Barth** for being on my committee, reading my thesis, and providing useful comments. I got to know both of them pretty well throughout my time here at UC-Riverside. Heather was a great mentor figure and will continue to be someone I look up to. Nic allowed me to TA field camp for him in the summer of 2016, which was a fun experience and taught me a lot more about

field geology.

Others have also contributed to my great experience here at UC-Riverside...

Pete Sadler was also a great mentor figure, helping me with TA-ing GEO-001, and allowing me to make changes to the labs and letting me also TA the spring field class with him.

Jerlyn Swiatlowski and **Nader Shakibay-Senobari** are apart of the 'Fun'ning group and provided me with useful advice and questions during our weekly group meetings. Jerlyn also became one of my best friends during this time and some people say you never see one without the other! If it weren't for her, I would have not known half of the useful information about applying for conferences and funding, campus activities, etc..

All of my office mates (Kuntal, Matt, Baoning, Bo, and Nader) were also great to have around. To talk to when I wanted to be distracted and becoming friends! The others outside the office that became good friends include Allie, Jozi, and Xueying and will continue to be friends for long after!

ABSTRACT OF THE THESIS

Searching for the Geodetic Signature of Wastewater Injection
at The Geysers Geothermal Field

by

Rachel LeeAnn Terry

Master of Science, Graduate Program in Geological Sciences
University of California, Riverside, March 2019
Dr. Gareth Funning, Chairperson

The Geysers geothermal field in northern California has seen subsidence, attributed to net volume loss during power production, since at least the 1960s. Over the last three decades this has been accompanied by reductions in reservoir steam pressure and power generation. To combat these effects, wastewater has been injected in the field since 1997. In order to better understand the effects of variations in production and wastewater injection on geothermal reservoir volume and surface subsidence over time, two continuously-recording GPS stations (TG01 and TG02) in the northern Geysers in 2012 and one in the southern Geysers (TG03) in 2013 were installed in the field.

In this thesis, I will present our first analyses of the continuous GPS data and our first attempt at modeling the data. Both TG01 and TG02 show early periods of uplift and later subsidence while TG03 shows ongoing subsidence. Next, we downsample steam extraction and injection data onto a rectangular grid and calculate observed

monthly volume changes as a function of position. We then use these to drive a forward elastic dislocation model to predict surface deformation changes each month in The Geysers field. The models cannot reproduce the GPS data, specifically the uplift that occurs at TG01. We then compare the observed volume changes with inverse elastic dislocation models of the volume changes required to reproduce the GPS time series. Due to low spatial resolution, we compare the total volume change in the field, which is comparable amplitude, and shows periods where the peaks are in phase, and periods where they are out of phase. In these cases, the peaks in the inverse modeled volume changes lag those in the reported data by one month. These 'out-of-phase periods' correlate with periods of peak injection in the field, typically in the winter and early spring months, suggesting that the GPS data are detecting a delayed deformation response to injection in the field, possibly related to the finite permeability of the geothermal reservoir rocks.

We also look at a case study of The Geysers M_w5.0 earthquake. This earthquake is a rare small shallow strike-slip earthquake capable of producing surface displacements. Our three continuous GPS stations in the field recorded coseismic displacement of up to 2 cm. We also were able to see the earthquake displacement in a 6-day descending interferogram. We ran forward and inverse models of both nodal planes provided by earthquake catalogs and found that both nodal planes produce consistent deformation patterns although the inverse model closely matched the NNW-striking nodal plane.

Contents

List of Figures

List of Tables

Chapter 1

Introduction

Geothermal energy has the potential to play a vital role in the transition to a renewable energy economy in the western United States and across the world. One of the key qualities about geothermal energy is that is a baseload source. This means that regardless of conditions, the geothermal plant can produce energy 24-hours per day. Other renewable energy sources are transient and can strain the power grid, thus geothermal is vital in pushing renewable energy to the forefront.

If managed improperly, geothermal can be a limited resource. It is important to understand and improve upon our ability to extract geothermal energy without depleting the resource to unusable levels. The extraction of water or steam from a geothermal reservoir without significant recharge reduces steam pressure and its capacity to generate electricity. Efforts in geothermal fields around the world to combat this issue primarily includes reinjection of extracted water or steam or the

injection of wastewater from nearby areas. Reinjection increases the sustainability of the field by supplying the reservoir with the fluid it needs to maintain its electrical generating potential.

The largest producer of geothermal energy in the world lies about 75 miles north of San Francisco, California and is known as The Geysers geothermal field. The Geysers has been in commercial operation since 1960. In its early history, power production at The Geysers steadily increased, reaching a peak of $\sim$ 2 GW in 1987 and then a more notable decrease in power production/shut down of power plants in the late 1980s and early 1990s (Figure 1.1). The reduction in power output is a result of declining steam pressures (3.4 MPa to 1.2 MPa) within the reservoir and is assumed to be due to production volumes and rates exceeding restoration of reservoir volumes by natural means (Gettings et al., 2002; Calpine, 2018). Evaporative steam loss is common in geothermal fields and can impact the long-term sustainability of the field.

Surface subsidence has been monitored at The Geysers over the past few decades by geodetic means. In the 1970s, leveling surveys indicated surface subsidence of up to 13 cm in 4.5 years in the area of highest steam withdrawals (Lofgren, 1978). In the 1990s, Mossop and Segall (1997) revisited previous leveling monuments with GPS receivers and measured subsidence rates of up to 4.8 cm/yr. Most recently, campaign GPS surveys recorded a reduction in subsidence rate following the introduction of wastewater pipelines into The Geysers field, with the most significant velocity changes occurred within 1-2 km of large injection sites (Floyd and Funning, 2013).

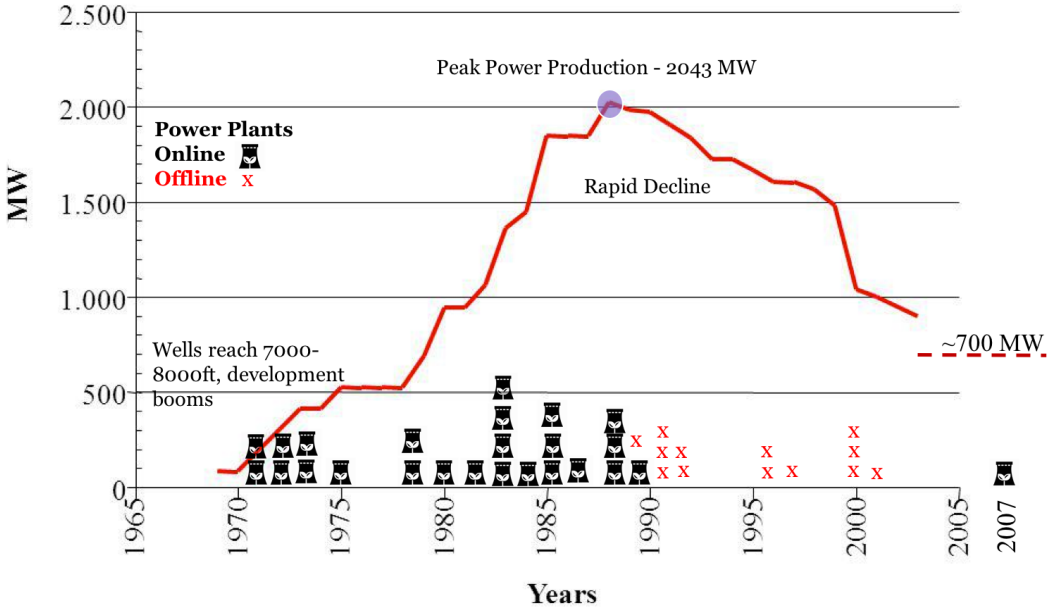

Figure 1.1: Power production at The Geysers geothermal field since 1970. A rapid increase in power plant production occurred throughout the 1970s and 1980s, reaching a peak of 2043 MW in 1987. However in the 1990s the field experienced a rapid decrease in steam pressure and power production. Production has currently stabilized at around 700 MW (figure modified from Capetti (2006))

The two wastewater injection pipelines, completed in 1997 and 2003, deliver an average of 15 million gallons per day to The Geysers area and were installed to combat the declining steam pressures. Since introduction of these pipelines, energy production has stabilized and as of 2017, the average output was 648 MW (Calpine, 2018). Due to the episodic nature of GPS campaign measurements (typically separated in time by multiple years), much was not known about the time dependence of subsidence/uplift due to production activities on shorter, daily-to-monthly time scales. Therefore, in December 2012, Floyd and Funning (2013) installed two continuous GPS stations in The Geysers field, and added another one GPS station in December 2013.

In this thesis, I present the continuous GPS data from 2012-2016 at The Geysers geothermal field installed by Floyd and Funning (2013). The goal of this project is to try to understand the connection between the geothermal reservoir and surface deformation. If the connection can be made, GPS can be used as a tool to monitor geothermal fields in the future and can aid in planning of infrastructure. By using GPS as a monitoring device, the plant operators have the chance to see where the reservoir is most susceptible to changes and can make informed decisions moving forward. The Geysers geothermal field is uniquely large and complex. By better understanding this field, GPS can be easily implemented in smaller geothermal fields around the world

In this review of the current literature, I will begin by discussing the varied history of The Geysers and its transition to a geothermal field. I will then talk about the geologic setting, history of surface deformation measurements, how surface deformation is modeled in geothermal fields, and about the on-going seismicity in the field. Chapter 2 will present and discuss our work with the continuous GPS data in the field and our first attempts to model the displacement. In chapter 3, I will present a case study of The Geysers M_w5.0 earthquake that occurred on December 14^{th}, 2016.

1.1 History of the Geysers geothermal field

The Geysers area has a long history, beginning around 12,000 years ago in the Palaeoindian period, when the first Native Americans arrived to the area (Hodgson, 2010). When settlers arrived in the mid-1800s, there were six Indian tribes living in distinct areas across The Geysers with their own distinct languages and cultures (Hodgson, 2010), utilizing the hot springs and mineral rich waters as sacred ceremonial sites and for healing properties. In the 1850s, The Geysers Resort Hotel was constructed and became increasingly popular over the years, with many wealthy and famous people, including Presidents Ulysses S. Grant and Theodore Roosevelt, visiting the resort. In the early 1900s, the popularity of the hotel dwindled, but the era of harnessing the geothermal power began.

In 1920, John Grant, a local entrepreneur, leased an area of The Geysers near a popular steam vent called 'The Witches Cauldron' to drill a well in an attempt

to harness the natural steam (Hodgson, 2000). The well, 'well No. 1', experienced a blowout at a shallow depth, and driller Glen Truit said, "the well blew up like a volcano" (Hodgson, 2000). A second well was more successful, finding steam at around 200 ft. Grant went on to develop a 35 kW power-plant, drilling eight steam wells between 1921 and 1925, that ran for a decade before failing due to technical issues, costs, and the rise of oil (Hodgson, 2000). Soon after in 1938, the hotel, now a sanatorium, burned down in a fire and there was a push to turn the area into a national monument (Hodgson, 2010). Theodore Roosevelt had toured the area in 1903 along with Yosemite Valley, and during his presidency created 150 national forests, 5 national parks and 18 national monuments, but it is unknown why The Geysers was excluded (Hodgson, 2010).

It was not until the mid-1950s that generating electricity via geothermal energy returned to The Geysers area, as the first modern geothermal wells were drilled and a contract with the Pacific Gas and Electric Company was signed (Hodgson, 2000). During the 1960s, power generation grew to 100 MW. At the time, majority of the steam generated escaped to the atmosphere and any condensate was released on the ground surface (Sanyal and Enedy, 2011). It was not until the 1970s that the practice of injecting condensate, now common in geothermal fields, began. The Geysers installed capacity grew steadily for the first 20 years of production, but by the 1980s, when prices for oil increased (post oil shock in 1979), The Geysers installed capacity

grew quickly, reaching 1,830 MW in 1986, and generating about 1,500-1,600 MW (Sanyal and Enedy, 2011).

Being the pioneer of geothermal energy in the United States, operators at The Geysers learned a hard lesson when steam pressures in the field began to decline rapidly, ultimately leading to shutdowns of a string of power-plants in the 1990s. Out of an installed capacity of 2,093 MW, in 1991 the electricity generation was only 1,326 MW, and by 1997 it had declined to 824 MW (Hodgson, 2000). It is thought that the steam pressure decline was due to overproduction of the reservoir without adequate time for restoration (Gipe, 1990). This decline led to a new era of attempts to stabilize The Geysers declining electricity production by increasing the steam pressure within the reservoir.

In 1991, The California Energy Commission formed a Technical Advisory Committee for The Geysers field and provided recommendations for increasing the life of the field, including injecting water from outside the field to replace what has been lost within the reservoir (Goyal, 2007; Brophy et al., 2010). Prior to this, re-injected steam condensate recycled about 25% of the total extracted steam (McLaughlin, 1981). In 1997, the first injection project was completed, piping wastewater from Lake County in what is known as the Southeast Geysers Effluent Pipeline (SEGEP). By 1999, electricity output from The Geysers field increased to about 1,000 MW (Hodgson, 2000). Just a few years later, in 2003, a second project, called the Santa Rosa Geysers Recharge Project (SRGRP) began delivering wastewater from the city of Santa

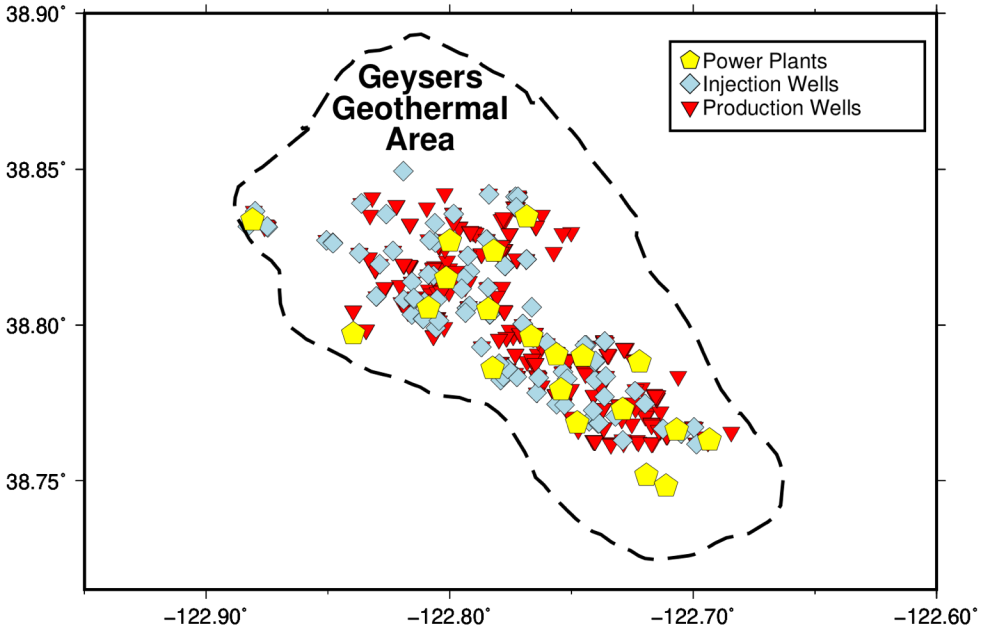

Figure 1.2: An up-close view of The Geysers geothermal area, including the 396 production wells (triangles), 96 injection wells (diamonds), and 22 power plants (pentagons). Typically around $\sim$ 75% of wells are in use at any one time.

Rosa to The Geysers field. Today, these two pipelines deliver about 15 million gallons per day of wastewater to The Geysers, and the field has since stabilized, with a current output of 648 MW (Calpine, 2018). The Geysers currently has 396 drilled production wells, 96 drilled injection wells, and 22 power plants (Figure 1.2).

1.2 Geologic setting

The Geysers geothermal field is located in what is commonly known as the Geysers–Clear Lake region. The mountainous topography of the region, which is a portion of the broader Northern California coast ranges, has a complex geological history. Late

Mesozoic subduction of the Farallon plate formed the Franciscan Complex that makes up much of the Geysers–Clear Lake region's bedrock geology (Atwater, 1970). The Franciscan Complex (described in detail by Bailey et al. (1964)) consists of sedimentary and metasedimentary rocks scraped from the subducting Farallon plate (Bailey et al., 1964; Stanley and Blakely, 1995) in the late Mesozoic and today hosts The Geysers geothermal reservoir. At The Geysers, the Franciscan Complex is primarily composed of greywackes and argillite (metashale), with greenstone and serpentinites intermixed (McLaughlin and Ohlin, 1984; Stanley and Blakely, 1995; Moore et al., 1995). As subduction of the Farallon plate continued along the western margin of North America, a collision occurred between the East Pacific Rise and the trench at $\sim$29 Ma in the area of the Mendocino fracture zone, giving rise to the current Mendocino triple junction and the San Andreas transform fault system (Atwater, 1970).

More recent activity in the Geysers–Clear Lake region is dominated by volcanism, with the region being the northernmost volcanic field in a north-south chain east of the San Andreas fault (Johnson and O'neil, 1984). Surface eruptions begin in the region at $\sim$ 2.1 Ma and continued until 10 ka, with eruptive materials consisting of mostly dacite (50%), rhyolite (20%), andesite (5%), and basalt (25%) (Johnson and O'neil, 1984; Hearn Jr et al., 1995). The melt is hypothesized to be from slab window asthenospheric upwelling when the Farallon slab broke off and continued subducting into the mantle (Schmitt et al., 2003)

Today, the region is dominated by tectonically active northwest-trending faults, most notably the Maacama Fault zone in the west, the Collayomi fault zone in the east and the Bartlett Springs fault zone in the northeast. Normal, thrust and strike-slip faults have been mapped in the region and the normal faulting has resulted in a series of horst and graben structures, most notably the Mayacamas mountain range representing a large horst structure (Chapman, 1975). As a result of being scraped off the subducting Farallon plate, volcanic activity and faulting, the rocks that lie within the Franciscan complex are fractured, sheared and characterized by weak metamorphism (McLaughlin, 1981). They also underlie parts the Great Valley rock sequence, which was thrusted over during collision. A pluton, as observed by gravity (Isherwood and Chapman, 1975; Stanley and Blakely, 1995), magnetic (Stanley and Blakely, 1995; Stanley et al., 1998) and seismic data (Gritto et al., 2013) , first encountered at depths >700 m below the surface (Schmitt et al., 2003) is responsible for the high heat flow at The Geysers. The fault-bounded fractured meta-graywacke in the Franciscan Complex above it allows for a steam-dominated geothermal reservoir to exist there.

1.2.1 The Geysers geothermal reservoir

The Geysers geothermal reservoir is one of the largest known geothermal reservoirs in the world, with an area in map view of ~ 100 km^2 (Mossop and Segall, 1997). It is a vapor-dominated system with evidence of widespread hydrothermal alteration

(Lockner et al., 1982; Jeanne et al., 2014). Hydrothermal fluids in the reservoir are stored and transported within a northwest trending vertical fracture network with well data indicating that these fractures are clustered between impermeable areas and may connect laterally (Thomas et al., 1981; Lockner et al., 1982). The main reservoir fluids are predominantly isothermal, with temperatures of 240°C, although well data indicates that a shallow high temperature zone exists below the main reservoir in the northern part of the field, with temperatures exceeding 350°C (Stark, 2003). Underneath the fractured reservoir lies a felsite layer, and above is a tightly sealed cap rock, impeding the flow of meteoric water into the reservoir (Lockner et al., 1982) (Boyle and Zoback, 2013).

1.2.2 The northwest Geysers Enhanced Geothermal System (EGS) project

Enhanced Geothermal Systems (EGS) utilize areas of high heat flow to manufacture a geothermal system. There are three requirements to maintaining a geothermal system – high temperatures, water or steam, and a fracture network. In areas with high heat flow at depth but with little conductive networks or permeability, geothermal engineers inject fluid to increase permeability and create a fracture network for the injected fluid to travel through. After successfully creating the network, a production well is drilled to intersect the network and allow the heated fluid to be pumped back to the surface, ultimately creating a loop.

The Department of Energy and Calpine began an EGS project in the northwest portion of The Geysers geothermal field in 2011. This area of The Geysers is unique because underlying the main geothermal reservoir is a high temperature ($\sim$ 400°C) zone with a less connected fracture network. Prior to this attempt, an EGS project was explored in the 1980s but was abandoned due to high concentrations of non-condensable gases which will corrode the wells (Garcia et al., 2016). Two wells (Prati State 31 and Prati 32) previously abandoned in the first exploration were reopened and deepened. Prati State 31 was set as a production well and Prati-32 was set as an injection well. The goal of the project was to inject fluid, creating a network of fractures in the high temperature reservoir, reduce concentrations of non-condensable gases, and provide a steam supply to the production wells nearby (Garcia et al., 2016). The injected water was brought in from the SRGRP.

The EGS project was able to increase reservoir pressure in comparison to the 1980s as well as reduce non-condensable gas concentration at the closest production well (P-25) (Garcia et al., 2016). At this well there was also an increase in flow rate and a small increase in power production (Garcia et al., 2016). A distinct surface uplift (up to 1 cm) was measured using synthetic aperture radar (SAR) in the area surrounding the injection site (Rutqvist et al., 2015). Soon after injection began, seismicity clustered in time/space indicated that there was an opening of new permeable zones and that these zones were oriented N130 (Garcia et al., 2016). It also showed NE and SW linear seismicity boundaries along known surface faults, indicating that faulting inhibits flow

to the NE/SW portions of the field (Garcia et al., 2016). By 2015 there had been a total of eight earthquakes $\geq M_w 2.5$ with the largest being a $M_w 3.7$ event that was associated with the EGS project. Ultimately, a high concentration of non-condensable gases resulted in Prati State 31 well casing to become corroded and be put on hold. There is continued injection at Prati 32 and production at P-25. The last phase of the project is to monitor the long-term effect of the EGS project.

1.3 Using geodesy to monitor surface deformation

1.3.1 The Global Positioning System

Alongside its use in civilian or military navigation, the Global Positioning System (GPS) is also a common geophysical tool to measure deformation of the Earth's surface at a precision of a few millimeters. As of November 2018, there are 31 operational GPS satellites, which fly in six orbital planes in medium Earth orbit (20,200 km) circling twice per day (GPS.gov, 2019). Locating one's point position on Earth using a GPS receiver requires a minimum of four satellites, three for position and one for clock offset. The information they receive from the satellite include encoded orbital parameters (satellites' positions in space) and clock time. The pseudorange, calculated by the receiver, is the distance measurement between the satellite and the receiver calculated by multiplying the difference in satellite clock time and receivers local time by the speed of light. (Blewitt, 2007). Receivers use these pseudoranges

to determine their position by trilateration (Blewitt, 2007). With this method and a low cost GPS receiver, the user's point location precision is on the order of a few meters (Blewitt, 2007).

For geodetic grade GPS, in which greater precision is desired, both a more accurate position of each satellite and a more precise estimate of the pseudorange between each satellite and the receiver is needed. For the former, the International GNSS Service (IGS) provides high-accuracy orbital parameters and reference station data. For the most accurate orbit positions and time, it typically takes between 12-18 days (Blewitt, 2007). More precise pseudoranges are obtained by recording the dual-frequency (L1 = 19 cm and L2 = 24.4 cm) carrier phase signal, which calibrates ionospheric refraction delay (Blewitt, 2007). The processing software we use is the GAMIT / GLOBK software suite (Herring et al., 2010), which uses a double differencing technique. This involves differencing the signals received from pairs of satellites and from pairs of ground stations, eliminating the biases in both the satellites' and receivers' clock times, both potential sources of systematic error in the estimated position of each station. As of now, with 24 hour RINEX files and the most accurate orbits, we can measure a point to a precision of 2 mm horizontal and 6 mm vertical (Blewitt, 2007). The difference in error is due to the satellites position in the sky. The lateral component of troposphere delay – the delay of the GPS signal caused by refraction through the troposphere, a potential source of error in GPS positioning – partially cancels out as the satellite flies in a semi-circle above the receiver, passing at the same

angle twice per day, from opposite directions. The vertical component of troposphere delay however, does not cancel, as the satellite only passes over once in the vertical position.

1.3.2 Interferometric Synthetic Aperture Radar

InSAR (interferometric synthetic aperture radar) is a technique for measuring ground surface displacements using radar images. SAR satellites fly in sun-synchronous polar orbits and acquire images periodically, a few days to a few weeks apart in time. By the use of long wavelength microwaves, the radar pulses are not affected by clouds. The satellites are equipped with an antenna that shoots pulses of radar, and as the satellites orbit, one point on the ground surface will be measured multiple times. These measurements are stacked, allowing the image to have a finer resolution due to the large apparent antenna length. The radar pulses send back information about each point on the ground – phase and amplitude. The phase is a function of the distance from the satellite to the ground and amplitude is related to the roughness and slope of the ground. After the same location on the Earth's surface is measured twice, the two SAR phase images can be differenced. Any differences seen can be related to surface deformation, particularly notable after large earthquakes or mass movements but can also be used as a long time series to measure small movements over long time scales (e.g. fault creep, geothermal/aquifer deformation). The resulting image is called an 'interferogram' and will show phase-difference fringes where

surface displacement has occurred. The change in phase is related to the wavelength of the radar and the distance that the ground moved, with each fringe representing a displacement of half of the wavelength in the radar line-of-sight direction (Pritchard, 2006). As the radar satellites have antennas that point at a steep angle (e.g. $\sim 30^{\circ}$ from the vertical) to the right of the flight direction, using both the ascending (south to north) and descending (north to south) orbits will allow you to distinguish between horizontal and vertical motion due to the opposite look directions from the satellite to the ground, as vertical motions will appear similar from both orbits, but horizontal motions will have opposite signs depending on the orbit direction.

1.3.3 Monitoring surface deformation at The Geysers

Notable subsidence was first identified in the mid-1970s in The Geysers, 14 years after power generation began. Between 1970 and 1975, seven power-plants were put online, beginning the era of large-scale power generation. Prior to the 1970s, there were very few studies connecting the extraction of fluids within geothermal reservoirs to ground subsidence, although there was extensive research connecting subsidence to groundwater pumping for other resources, e.g. oil, gas, groundwater (Phillips et al., 1975). Interestingly, it was suggested by Bowen (1973), that vapor-dominated fields, like The Geysers, may not be affected by subsidence due to the constant temperature and pressure. We now know that subsidence does affect all types of geothermal field (Massonnet et al., 1997; Carnec and Fabriol, 1999; Fialko and Simons, 2000; Oppliger

et al., 2005; Eneva et al., 2011; Ali et al., 2016), and has guided the production history at The Geysers geothermal field.

The first geodetic benchmark network in The Geysers was set up by the United States Geological Survey (USGS) and the National Geodetic Survey in 1972–1973 to measure production effects (Lofgren, 1978). Lofgren noted four deformation effects that may be indirectly or directly related to fluid withdrawal – vertical and horizontal compression of the reservoir, thermal expansion or compression, landsliding or mass wasting by induced seismicity, hydraulic stress triggered earthquakes on natural faults in the area (Lofgren, 1978). One concern in measuring deformation due to production effects is that The Geysers is in an active tectonic region, and thus the network was referenced to benchmarks outside of the production area assumed to be stable and with their elevation fixed for each survey (Lofgren, 1978). Using first-order leveling (vertical) and electronic distance measuring equipment (horizontal), they measured for movement along transects beginning in 1972 and ending in 1977. Horizontal movement, consistent with compression, ranged from 15 mm/yr in the areas of highest production to 4 mm/yr in the surrounding area (Lofgren, 1978). Vertical subsidence measurements were also seen near power plant production areas at rates of 40 mm/yr from 1973–1975 and 20 mm/yr from 1975–1977 (Lofgren, 1978). Changes in reservoir pressure (-180 psi from 1969–1977), correlated spatially (Figure 1.3), in time, and in magnitude with the measured subsidence, suggesting a direct relationship (Lofgren, 1978; Lipman et al., 1978).

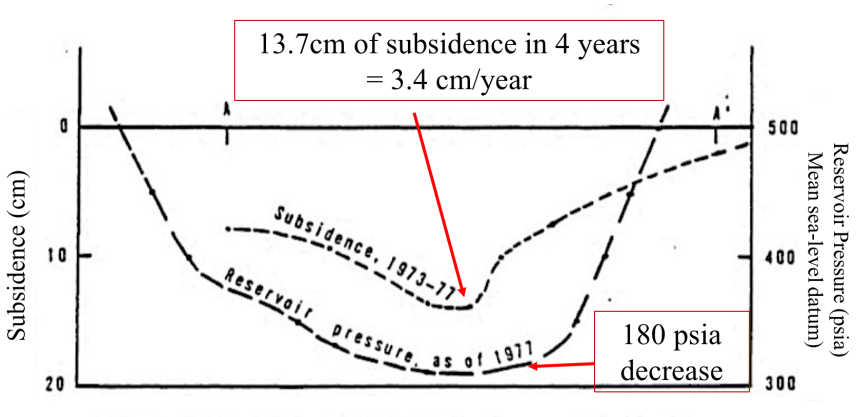

Figure 1.3: Subsidence along a transect from a NW to SE transect across The Geysers reservoir from plotted alongside reservoir pressure data from (Lipman et al., 1978) showing the relationship between reservoir pressure decline and subsidence. Figure edited from Lofgren (1978).

It was not until the 1990s that the geodetic benchmark network installed in the early 1970s and measured using leveling by Lofgren (1978), was measured again to study the effects of geothermal production. The Global Positioning System (GPS) began to be routinely used as a geophysical method in the early 1990s, and thus Mossop et al. (1997) used this method to remeasure the geodetic network. By this time, The Geysers had experienced its significant decline in reservoir steam pressure and power production. Mossop et al. (1997) completed campaign GPS surveys in 1994, 1995, and 1996, measuring 30–40 benchmarks (twice) during each survey (Mossop et al., 1997). The maximum rate of subsidence observed between 1977 and 1996 was at benchmark P244, with a rate of 4.7 $\pm$ 0.2 cm/yr., and located 2 km north of the maximum subsidence measured during 1973–1977 (Mossop et al., 1997). The study found that much of the subsidence was consistent with the known extent of

the geothermal reservoir and little subsidence was found outside of this area (Mossop et al., 1997).

Post-SEGEP and prior to SRGRP injection projects, more campaign GPS measurements were taken as part of a high-precision gravity survey of The Geysers reservoir. Three gravity and GPS surveys were conducted between September 2000 and September 2001 and found that in the center of the production field, the stations showed an annual average subsidence of 2 ± 2 cm (Gettings et al., 2002). Between September 2000 and April 2001, stations in the center of the production field showed an annual average subsidence of 3 ± 2 cm, with an average rate of 4.5 cm/yr. and a range of 1–8 cm (Gettings et al., 2002). Between April and September 2001, GPS measurements showed less subsidence (1 ± 2 cm/yr.) (Gettings et al., 2002). Gravity changes during the period showed an average of -38 ± 8 μGal with an average change of $-10 \pm 8\mu$Gal. Extraction was higher for the months of September to December 2000, and the GPS and gravity data may reflect this, but overall, the net extraction was the lowest for the months between January 2001 and March 2001.

Floyd and Funning (2013) continued these campaign GPS surveys, taking GPS measurements in and around The Geysers production area in 2009, 2010, and 2011. Between the previous measurements in 1996, 2001, and 2006, both injection projects had begun, delivering about 15 million gallons per day of wastewater to The Geysers. The GPS time series showed an overall decreased rate of subsidence from the 1990s to the 2000s, with the most statistically significant changes lying within 1-2 km of large

changes in injection (Floyd and Funning, 2013). Floyd and Funning also installed three continuous GPS stations, two in December 2012 (TG01 and TG02) in the northern portion of The Geysers field, and one in December 2013 (TG03) in the southern portion of the field. An analysis of this continuous GPS data will be shown later in this thesis, but shows a complex history of deformation including periods of both uplift and subsidence occurring in the field since installation. Interestingly, the uplift occurs at the closest GPS station (TG01) to the EGS project in the northwest Geysers.

A study by Vasco et al. (2013), used InSAR to quantify surface deformation at The Geysers. They looked at two time periods, 1992–1999 and May 2011–April 2012. For the earlier time period, they used C-band data from the ERS-1 and ERS-2 satellites, with a density of permanent scatters of 12 per square kilometer. They found subsidence, with a peak range-change velocity of 50 mm/yr, consistent with previous leveling and GPS data. For the 2011-2012 data, they commissioned the X-band SAR satellite TerraSAR-X to look for deformation associated with the EGS project in the northwest Geysers. The data overlapped spatially with the previous InSAR data, but had higher resolution (1122 per square kilometer). There was spatial variation consisting of subsidence and uplift. The uplift observed was between the EGS injection and production wells and was on the order of 10 mm. Jeanne et al. (2014) also looked at the Terra-SAR-X satellite data from May 2011–September 2012. They found that the deformation (uplift and subsidence) trended along a $\sim 130°$-

striking zone, consistent with shear zones found previously (e.g. Hulen and Norton, 2000).

1.4 Surface deformation modeling

1.4.1 Geothermal systems

Surface deformation is common in geothermal fields and can be caused by reservoir volume loss/gain, poroelastic compaction, and thermoelastic effects. There have been many attempts to model the deformation at multiple geothermal fields, including Brady (Oppliger et al., 2005; Ali et al., 2016), East Mesa (Massonnet et al., 1997), Coso (Fialko and Simons, 2000), Cierra Prieto (Carnec and Fabriol, 1999) and The Geysers (Mossop et al., 1997; Mossop and Segall, 1999; Vasco et al., 2013; Jeanne et al., 2014; Rutqvist et al., 2015). Currently, the most common method used to measure surface deformation at geothermal fields is InSAR because of its capability to measure wide areas of deformation over time without the need to access the site, but is limited by satellite recurrence intervals and atmospheric noise. To model the deformation, most start out with relatively simple models (e.g. spherical 'Mogi' sources (Mogi, 1958), rectangular 'Okada' dislocations (Okada, 1985)) and invert for the volume changes required to produce the surface changes. Both models are commonly used to model magmatic and volcanic systems, but Okada dislocations are also used to model slip on faults.

1.4.2 Mogi sources

Mogi (1958) explored the relationship between ground deformation and eruption history at multiple active volcanoes by comparing leveling and triangulation data before and after eruptions. He found that deformation was similar in each eruption, with a wide circular area of depression assumed to be due to changes in the magma reservoir beneath and a sudden change nearby the volcanic crater, caused by the eruption of lava. By using the data obtained before and after eruption, Mogi showed that these changes could be explained by the movement of substances or changes in pressure at depth in the Earths crust. In this model it is assumed that the Earths crust is a semi-infinite elastic body, and that the deformation is caused by a spherical source with hydrostatic pressure. These theoretical pressure sources reflect a change in volume in the magma chamber and the resulting deformation depends on its horizontal position and depth, as well as the magnitude of the volume change.

1.4.3 Okada dislocations

The Okada model (Okada, 1985) is built upon the work of (Steketee, 1958), who first introduced dislocation theory to the field of geophysics. Okadas dislocation model (Okada, 1985) calculates displacements at the surface of an elastic half-space due to motion of a rectangular dislocation beneath the surface. This dislocation can be oriented in any direction (i.e. the strike and dip can vary) and is defined by its length, width and depth from the surface, as well as its mode of motion, which can

be strike-slip, dip-slip, opening/closing, or a combination of these. For the purpose of calculating surface deformation for magmatic systems, Okada dislocations with opening/closing motions are useful for representing dikes/sills but can also represent fluid-driven opening or closing cracks. Okada dislocations can be applied to geothermal reservoirs either by using horizontal (rock layer) or vertical dislocations (fluid-filled cracks).

1.4.4 Modeling deformation at The Geysers

There have only been a few studies considering the relationship between surface deformation and production activities at The Geysers. The first study by Mossop and Segall (1997) used 20 years of surface displacement data (leveling and GPS) to invert for volume change in The Geysers geothermal reservoir using Mogi point sources (Mogi, 1958). They found that three sources, located within the steam pressure lows, produced the most statistically significant fit to the displacement data; four sources provided no significant improvement. The three-source model had depths of 1.69, 1.72 and 3.05 km and volumes of 9.53×10^6 m^3, 1.55×10^6 m^3, and 6.42×10^6 m^3. They determined that a change in reservoir temperature due to the injected fluids could not explain the subsidence, but could be due to pore-pressure changes if the quasi-static bulk modulus was K $\leq 3.6 \times 10^9$ Pa. However, observed seismic velocities at The Geysers, (O'Connell and Johnson, 1991) and laboratory measurements of greywacke (Kern, 1982), suggested an order of magnitude higher K values. Once

considering that the greywacke has a fracture porosity of 1-2% the effective bulk modulus was consistent with the bulk modulus required to produce the observed subsidence (Mossop et al., 1997).

Mossop and Segall (1999) continued this work in inverting displacements in an elastic half space with internal volume strain rates, instead of Mogi sources. They divided the leveling / GPS measurements into four time periods, 1975–1980, 1980–1994, 1994–1996, and 1977–1996. The model grid contained four layers, with 288 cubic km elements in each layer. The inversion method tended to place volume stain as close to the surface as possible (which may underestimate volume strain), when it is likely to be dispersed. The checkerboard resolution test for the models indicated the highest resolution occurs in the center of the field where most of the surface measurements were taken and is less resolved outside of that area. Therefore, the main volume contraction is well-resolved. For the 1977–1996 model, the volume strain between 0–1 km is similar to mapped pressures indicating a direct relationship between volume strain and pressure. The other time periods also show spatial correlation with pressure values, but all models differ in magnitude. Similar to their previous study (Mossop et al., 1997), they suggest that the bulk modulus should be $< 4.6 \times 10^9$ Pa and can be accounted for by the fracture porosity of the rock.

More recent studies (e.g. Vasco et al., 2013; Jeanne et al., 2014; Rutqvist et al., 2015) have focused on the Enhanced Geothermal Systems (EGS) project in the northwest corner of The Geysers field. They model the northwest Geysers reservoir us-

ing the thermal, hydraulic, and mechanical numerical simulator, TOUGH-FLAC, ((Rutqvist et al., 2002, 2010; Rutqvist, 2011), under multi-phase flow conditions (Rutqvist et al., 2015). They measured surface deformation from the EGS injection wells using InSAR data from the TerraSAR-X satellites (Vasco et al., 2013; Jeanne et al., 2014; Rutqvist et al., 2015). The models contained four layers (0-6.5 km depth); a cap rock of unfractured greywacke, fractured greywacke hosting the normal temperature reservoir ($\sim 240°C$), hornfelsic biotite metagraywacke hosting the high temperature reservoir (up to $\sim 400°C$) and a granitic intrusion composed of felsite.

Vasco et al. (2013), modeled 180 days of injection and compared with the InSAR data and were unable to match the magnitude of deformation but could match the temporal variation. To model the magnitude correctly, the bulk modulus needed to be significantly higher. The aim of Rutqvist et al. (2015) was to compare pre-stimulation modeling predictions with data after the injection began. They used the surface deformation to estimate porosity, permeability and elastic modulus and determined that the heterogeneous nature of deformation suggested that more complex geological features are required to explain the deformation. When comparing the pre-stimulation model uplift with surface deformation from InSAR, they showed that when using the bulk modulus calculated for the previous 44 year subsidence history, the uplift would be significantly overestimated and needed to be increased from 3.3 GPa to 16–34 GPa. Jeanne et al. (2014) built upon the model of Rutqvist et al. (2015), but added more complex geology to their model by introducing two 15 m wide shear zone families

($\sim 130^\circ$ N and $\sim 050^\circ$ N trending), and modeled injection for 270 days. By adding this complexity, they were able to match the overall vertical deformation at the end of the 270 days for seven out of eight locations. The location that did not fit was due to an underestimated uplift. All three studies also corroborate the conclusion of Mossop et al. (1997) that thermoelastic contraction had little effect on surface deformation, which is mainly driven by poroelastic effects.

1.5 Seismicity at The Geysers

The Geysers geothermal area lies to the east of the seismically active Maacama–Rodgers Creek fault zone, west of the inactive Collayomi fault zone, and south of the active Konocti fault. Although the geothermal area lies within these fault zones, the area itself had little historical seismicity prior to production in the 1960s (Trugman et al., 2016). As of 1984, The Geysers had become one of the most seismically active areas in California, with ten $> M_w 0.5$ microearthquakes per day (Eberhart-Phillips and Oppenheimer, 1984). By this time, it was known that production activities at The Geysers were inducing earthquakes, but the mechanism for induction was unknown. Various mechanisms had been proposed – cooling fracture surfaces by reduction in normal stress (Denlinger and Bufe, 1980), volumetric change from steam withdrawal (Majer and McEvilly, 1979), and an increase in reservoir strength converting aseismic creep to stick slip motion (Allis, 1982; Eberhart-Phillips and Oppenheimer, 1984). There has also been discussion about whether the majority of the induced earthquakes

are production driven (Eberhart-Phillips and Oppenheimer, 1984) or injection driven (Johnson et al., 2016; Trugman et al., 2016). More recently, the literature on injection driven seismicity greatly outweighs the alternative and is also supported by injection induced earthquakes in non-geothermal areas (Foulger et al., 2018).

Today, the seismicity at The Geysers is still apparent, outlining the geothermal reservoir, occurring at shallow depths (< 6 km) and with magnitudes generally between 0 and 3, with the largest earthquake recorded being a M_w5.0 event (Figure 1.4). The rate of seismicity at The Geysers is 45 times higher than the nearby areas (Gunasekera et al., 2003). The background rate of seismicity from 1984 to 2003 was approximately 0.7 earthquakes per day, but increased to an average of 1 earthquake per day after the addition of the Santa Rosa injection pipeline in 2003 (Trugman et al., 2016). This background seismicity also reveals seasonal fluctuations, with peaks at times of increased monthly injection (Trugman et al., 2016; Johnson et al., 2016) and correlated with depth (Johnson et al., 2016). Johnson et al. (2016), found seismicity lagged with depth for up to 6 months reaching 3 km below the injection depth, consistent with gravity driven fluid migration and with the findings of Beall et al. (2010) where $> M_w$3.0 earthquakes peaked in the high temperature zone 3–5 months after peak injection.

Large earthquakes are a concern in geothermal areas and other areas injecting fluids into the subsurface. These earthquakes have the potential to shut down projects due to public concern and harm. The Geysers M_w5.0 earthquake was the largest

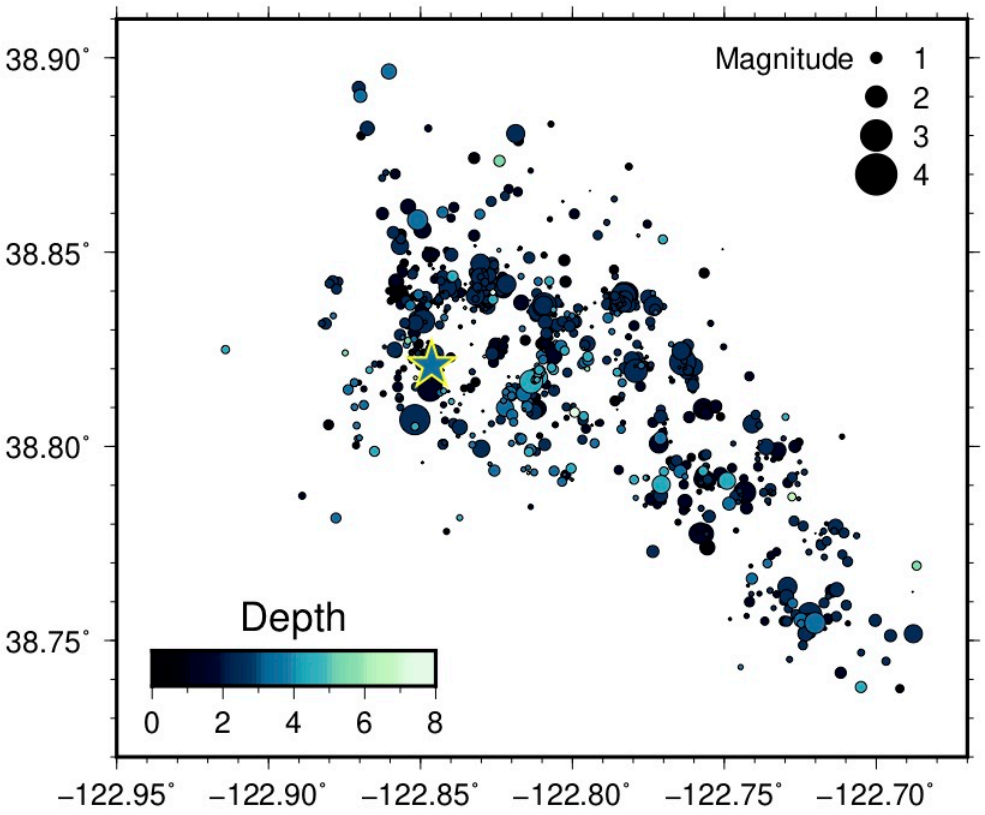

Figure 1.4: Distribution of earthquakes in one month (December 2016) at The Geysers, showing both magnitude and depth information. Most earthquakes that occur at The Geysers have magnitudes less than 3 and depths less than 6 km, indicating that most seismicity occurs within the geothermal reservoir. The star indicates the largest recorded event, a M_w5.0 earthquake on December 14^{th}, 2016.

earthquake to occur in the area since production started. There have also been 34 M_w4.0 and above earthquakes in the field. Events any larger in magnitude have the potential to cause structural damage in the area, and disrupt the power plant operations. It is important to understand the connection between geothermal activity and the potential for large seismic events.

Chapter 2

Working with GPS data from The Geysers

In this chapter, I present the first analyses of the continuous GPS data from The Geysers and our first attempts at using simple elastic dislocation models to reproduce the GPS displacement time series. We compute forward models using steam extraction and water injection monthly volume totals to predict surface displacements and inverse models using the monthly changes in vertical and horizontal positions from the GPS data to infer reservoir volume changes. We compare the model displacements with our GPS time series displacements each month to assess the fits of the models. We then compare the forward and inverse models' total volume changes each month in The Geysers. Based on our results, we also investigate a potential time lag in deformation response due to injection, production, or both.

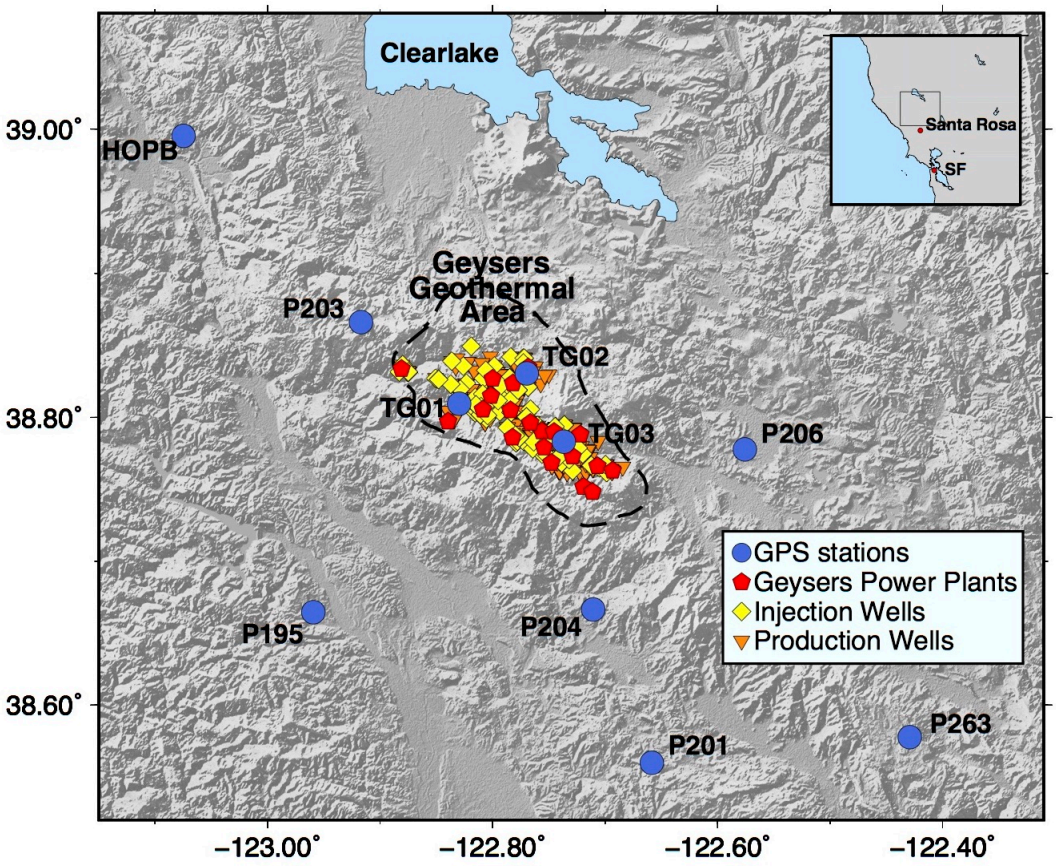

Figure 2.1: Overview of the Geysers geothermal field and surrounding area. The black dashed line outlines the Geysers geothermal reservoir area. Outside of The Geysers, the blue circles show the Plate Boundary Observatory continuous GPS stations and within the boundary show our three continuous GPS stations (TG01, TG02, TG03). Injection wells (yellow diamonds), production wells (orange triangles) and power plants (red pentagons) are also shown. Inset shows location of map area in context to surrounding area (black box). The Geysers geothermal field is located $\sim$ 75 miles (120 km) NE of San Francisco.

2.1 GPS data processing

Gareth Funning (University of California, Riverside) and Michael Floyd (Massachusetts Institute of Technology) installed two continuous GPS stations (TG01 and TG02) in the northern section of the Geysers geothermal field in December 2012 and January 2013 and a third (TG03) in the southern section in December 2013. These sites are telemetered and push data daily to the Northern California Earthquake Data Center at UC Berkeley, from where is it downloaded to MIT and processed. The daily data are processed using the GAMIT/GLOBK software suite (Herring et al., 2010), with IGS final orbits and atmospheric loading applied to improve accuracy and reduce scatter of the vertical component (e.g. Tregoning and Watson, 2009, 2011). Nearby sites from the Plate Boundary Observatory (e.g. 'P' sites in Figure 2.1) and other sites further afield in the western hemisphere are included in the processed network to stabilize the resulting time series in the terrestrial reference frame. The sites surrounding The Geysers are also used to define a local reference frame, where the velocities of the surrounding sites are minimized to reveal the motions within The Geysers relative to the immediate surroundings.

2.2 GPS time series

Daily vertical time series and cumulative horizontal vectors for each year relative to this local reference frame are shown in Figure 2.2 for our three sites in The Geysers.

It is immediately evident that the sites in the northern Geysers (TG01, TG02) show periods of uplift until around fall 2014, whereafter all sites subside from 2014 to 2016. The step in vertical time series at the end of 2016 is due to movement from The Geysers M_w5.0 earthquake on December 14th, 2016. All stations recorded both horizontal and vertical movement during the earthquake (Figure 2.2 and 2.3). The cumulative horizontal component deformation for TG01 and TG02 in Figure 2.2 shows inward motion, which is consistent with contraction of The Geysers reservoir. TG03, although moving slightly to the southeast, is also consistent with contraction due to more production taking place in the southern portion of the field. The east and north component time series are shown in Figure 2.3.

In this study, we focus on the period from December 2012– February 2017. During this time, the GPS station TG01, located in the northwest portion of the field record uplift of $\sim$ 40 mm from January 2013 to September 2014, subsidence of $\sim$ 25 mm from September 2014 to October 2016, and resumed uplift from October 2016 until February 2017. It also recorded continuous southward and eastward movement of $\sim$ 40 mm over the 4-year period. Station TG02, located in the northeast portion of the field recorded shorter periods of uplift and subsidence, of $\sim 10 - 20$ mm between December 2012 and September 2014 and then subsided $\sim$ 40 mm from September 2014 to November 2016, and had a short period of uplift of $\sim 5 - 10$ mm from November 2016 to February 2017. It also recorded an almost continuous southward movement of $\sim$ 50 mm but only $\sim$ 5 mm of eastward movement. The GPS station

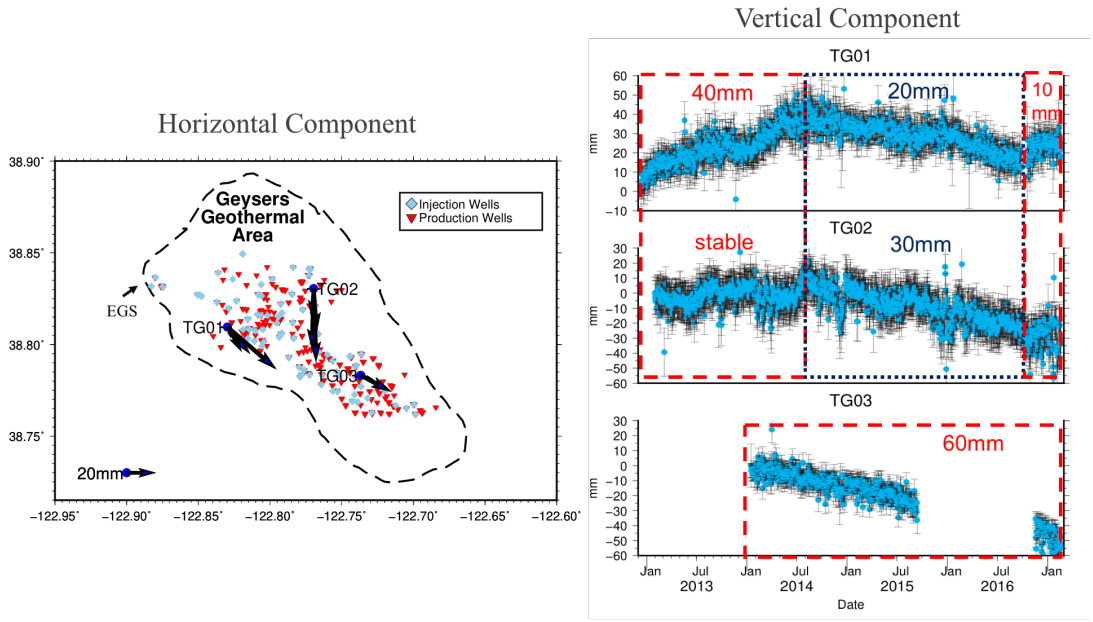

Figure 2.2: Cumulative horizontal displacement vectors (left) and vertical time series (right) for the three Geysers continuous GPS stations (TG01, TG02, TG03) for the period from December 2012–February 2017. Most notably, there was a period of uplift of $\sim$ 40 mm at TG01 in the northwest portion of the field closest to where the EGS project was located. Horizontal vectors are consistent with contraction of the reservoir.

TG03, the only station located in the southern portion of the field, was the last GPS station to be installed in December 2013 and was offline (cables = animal food) for the time period between September 2015 and December 2016. Despite the gap in time, TG03 showed overall subsidence of $\sim$ 60 mm and short periods of northward and southward movement of $\sim$ 10 mm, but an overall southward movement of $\sim$ 15 mm and eastward movement of $\sim$ 20 mm.

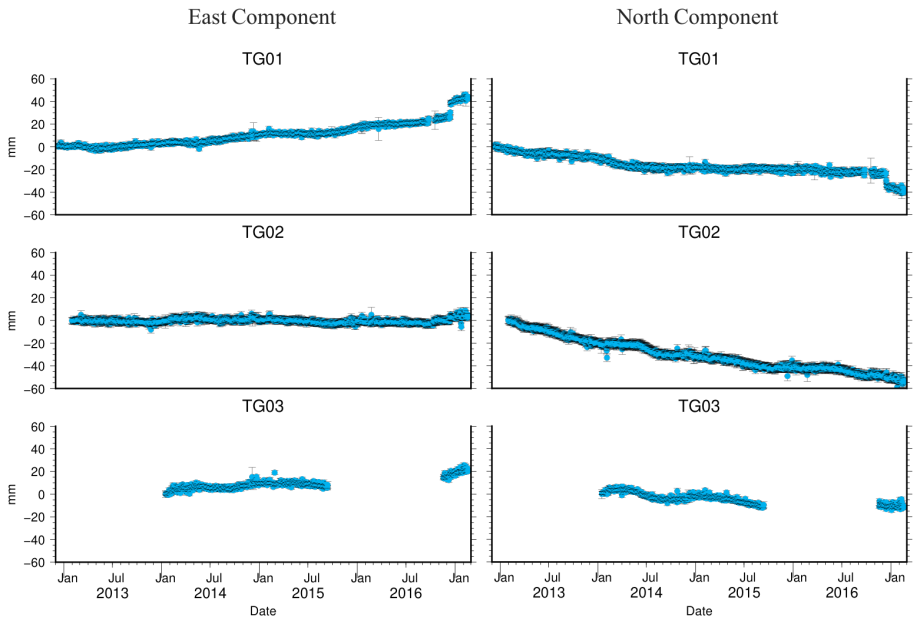

Figure 2.3: East and north component time series for the three Geysers continuous GPS stations (TG01, TG02, TG03) for the period from December 2012–February 2017.

2.3 Correcting for seasonal motions

A common signal in GPS time series data is seasonal motions due to hydrological loading, atmospheric loading, and snow/soil moisture mass loading. This signal is expected to be consistent over an area larger than The Geysers (Dong et al., 2002). To mitigate such signals, we remove a common seasonal signal estimated using common-mode filtering (Wdowinski et al., 1997) of data from six regional plate boundary observatory (PBO) GPS stations within 100 km of The Geysers geothermal area. We choose to forgo estimating long-term seasonal trends using principal component analysis due to the dramatic changes in climate over the last decade in California. The PBO station P203 (proximity shown in Figure 2.1) was not included as part of the

regional signal as its time series (Figure 2.5) shows abnormal movement during the time interval of the The Geysers northwest EGS demonstration project (Garcia et al., 2012), which is the type of local deformation signal we are attempting to retain while correcting for regional-scale fluctuations. The seasonal correction estimated using the other six PBO stations is shown in Figure 2.4. The average amplitude of seasonal loading in the region was on the order of ~ 5 mm. This step was important because injection rates are increased in the rainy season and we do not want to overestimate the effect it has in the models. The effect can be seen in Figure 2.4 by the reduction of high and low periods in the time series.

2.4 Steam extraction and water injection well data

Steam extraction (production) and water injection well data for years 2012–2016 were obtained from the California Department of Conservation, Division of Oil, Gas and Geothermal Resources (e.g. California Department of Conservation, Division of Oil, Gas, and Geothermal Resources, 2017). The California Department of Conservation requires that all geothermal well data be reported and publicly available each year. Each well is assigned an API, which is a unique and permanent numerical identifier, allowing well data to be consistently reported each year despite changes in name or ownership.

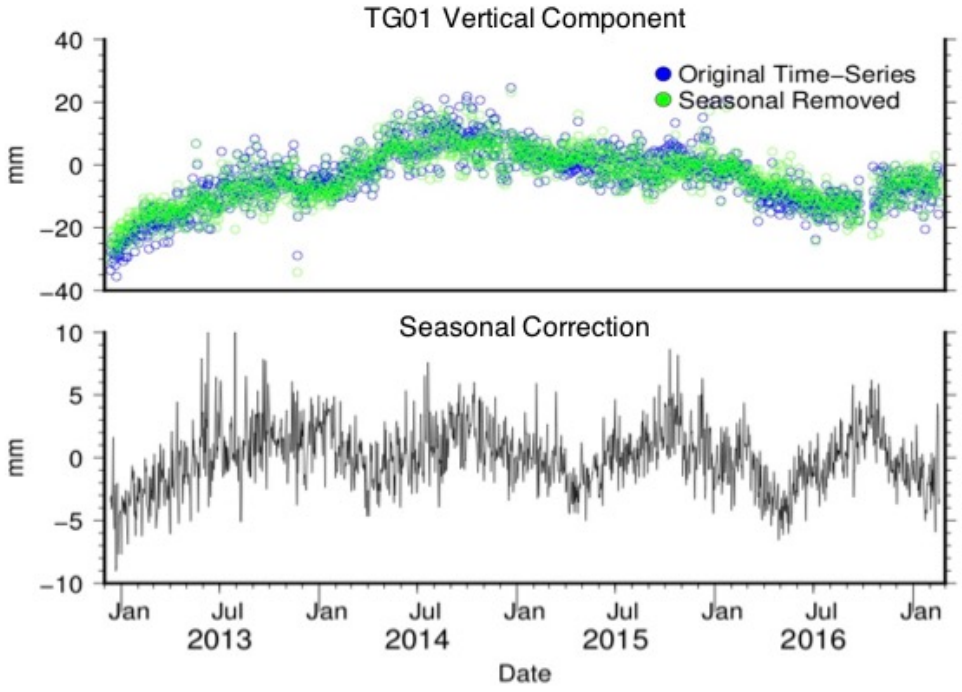

Figure 2.4: Correcting GPS time series for regionally-correlated seasonal motions. Top: The vertical component time series of the GPS station TG01 with (green) and without (blue) common-mode filtering of seasonal signals. The corrected GPS time series has reduced variation in position. Bottom: The seasonal correction (black), estimated using the six PBO stations within 100 km of The Geysers, shows an average seasonal loading amplitude of $\sim$ 10 mm.

The total numbers of drilled production and injection wells in The Geysers area are 396 and 96, respectively, but not all wells were in use during the 2012–2016 period. Since well records are reported on a monthly basis, our model data input is limited to monthly gross injected volumes and gross steam volumes. The total monthly production, injection and total (injection minus production) are shown in Figure 2.6. Water injection in The Geysers is seasonally modulated, with the greatest injection volumes in the winter season when precipitation is the highest. Production remains approximately constant over the four-year period and is larger in amplitude

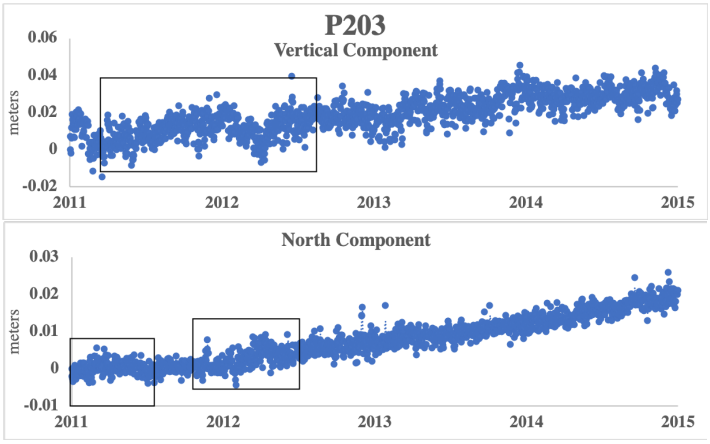

Figure 2.5: Vertical and north component time series for the PBO station, P203 which lies north of The Geysers geothermal field. P203 showed abnormal movement during the EGS period at The Geysers. In the vertical component, there was a prolonged period of uplift between 2011–2012 and a more prominent subsidence in 2012 than is recorded in the rest of the time-series after the EGS project was over. For the north component, there are velocity increases in its northward movement. After the EGS project, P203 resumes a stable northward trend. There was no noticeable change in the east component time series and thus is not shown.

than injection for almost all months. The EGS project, which ended just prior to the installation of our GPS stations in The Geysers can be seen to influence the total injection, particularly at the end of 2012.

To deal with the large number of wells in close proximity to one another and simplify the modeling process, we apply two downsampling approaches (Figure 2.7). First, we made a 1.5×1.5 km grid across The Geysers field, and second, we grouped the wells into three main areas (northwest section, north section and south section). We chose to split the north and south section due to changes in reservoir shape, and the northwest section was separated from the north section due to its geographically separation and its use in the EGS project. For the remainder of this paper, we will

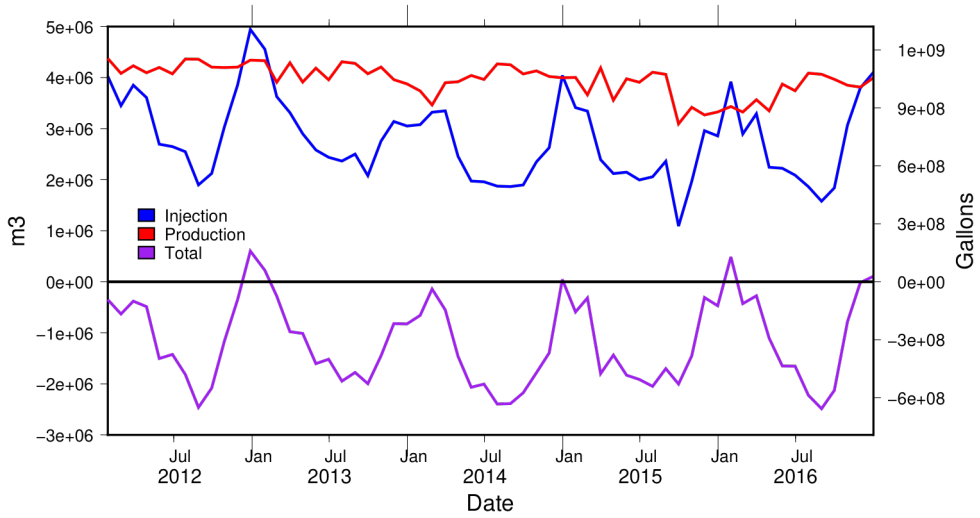

Figure 2.6: Total monthly production (red), injection (blue) and combined (injection minus production, purple) for all active geothermal wells within The Geysers geothermal field from 2012 to 2016. Injection is seasonally modulated with highest volumes in the winter months, while production remains approximately constant over the five year period. Production volumes are consistently higher than injection for almost all months during this time period.

refer to the 1.5×1.5 km grid as the 'fine grid' and the three-area grid as the 'coarse grid'. We sum monthly gross steam extraction and injection volumes for each grid cell and use these totals as inputs in our forward model calculations, described below.

2.5 Forward and inverse models

To assess the relationships between our time series of surface displacements, as measured by our GPS stations, and volume changes within the geothermal reservoir, we compute two types of model. We use our downsampled monthly injection and production volume data to calculate forward models of the surface deformation that

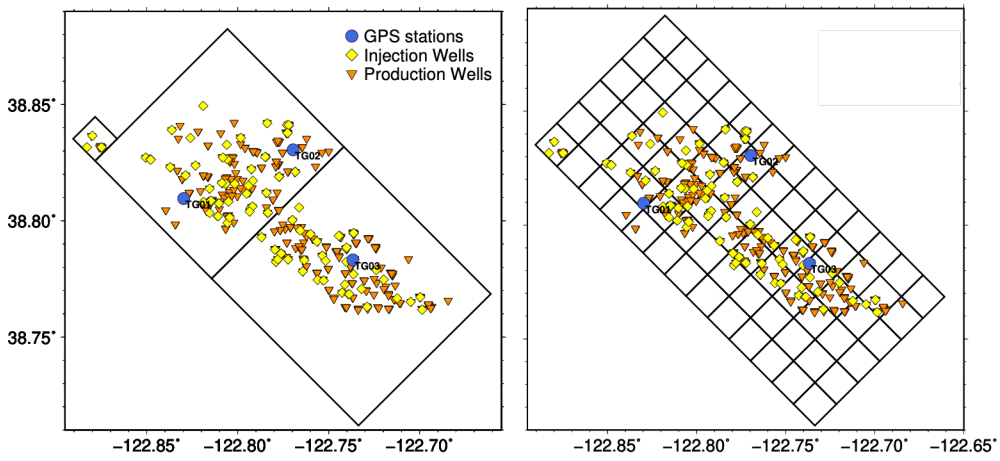

Figure 2.7: Two gridding schemes used to downsample well data, with a 1.5 x 1.5 km grid on the left (fine grid) and a three-area grid (coarse grid) on the right, indicated by black outlines. Each grid cell with wells was summed for their total injection and extraction volumes. Injection (yellow diamonds), production (orange triangles) and the three continuous GPS stations (blue circles) are also shown.

might be expected as a result. Then, we use our GPS deformation time series to estimate inverse models of the reservoir volume changes that best explain those data. In both model types, we compute Greens functions (Equation 2.1 relating reservoir opening to surface displacement, assuming opening on rectangular elastic dislocations within an isotropic elastic half space (Okada, 1985), one within each cell of our downsampling grids, testing the coarse and fine grids separately. For the matrix equation,

$$Gv = d \tag{2.1}$$

G is our Green's function matrix relating reservoir opening, in meters, to surface displacement from each dislocation to each GPS station location, v is our volume data

(km^3) converted to meters opening based on the length and width of the dislocations, and d is the model displacements for each GPS location. We test two alternative configurations of these dislocations within each cell – a horizontal opening sill, and a pair of conjugate vertical dikes. A visual representation of these dislocations is shown in Figure 2.9.

For the coarse grid, the location for each dislocation in each cell is centered on the effective 'center of mass' of volume change for that cell for the 48 month period,

$$X = \frac{m_1 x_1 + m_2 x_2 + ... + m_n x_n}{m_1 + m_2 + ... + m_n} \tag{2.2}$$

computed using the extraction and injection volumes (m) and their corresponding well locations (x). The surface length of each dislocation is the distance from the northernmost well to the southernmost well in each section and is 1 km for the northwest cell, 6.4 km for the north cell and 8 km for the southeast cell. For the fine grid, each dislocation is 1.45 km and each center is the geographic center of each grid cell. The width of each dislocation is 3 km and is based on the average width of the reservoir. The center of each dislocation is located at a depth of 3.5 km. We choose this depth to be in the middle of the known extent of the reservoir. The reservoir varies – from ∼0.3 km below sea level to 4 km below sea level (Mossop and Segall, 1997), and The Geysers area is mountainous with elevations up to 4 km. The vertical well depths (from surface) range from 162 m – 3915 m, with the average depth of ∼2200 m. The strike used for horizontal dislocation models is 335° and is based on

the NW-SE trending direction of The Geysers geothermal field and the strikes used for the two vertical dislocations are 335° and 65°. We assume a Poisson's ratio of 0.25 for all models.

2.5.1 Forward models

For each forward model, we input (separately) total injection and extraction volumes for each month, and, using the areas of the dislocations being modeled, estimate the amount of dislocation-normal displacement (opening or closing) required to match those volumes. We then use these to drive a dislocation model to compute the monthly vertical and horizontal surface displacements at each GPS station location for each grid cell and sum them to get the total predicted displacement for each month at each station. This monthly deformation is compared to our GPS time series for the same time period and a root-mean-square (RMS) misfit (Equation 2.3) is calculated to evaluate the fit, with $\hat{d}$ equal to the recorded GPS displacements, d equal to the modeling displacements and n equal to the total number of displacements.

$$\text{RMS misfit} = \sqrt{\frac{\sum_{i=1}^{n} \left(\hat{d}_i - d_i\right)^2}{n}} \tag{2.3}$$

2.5.2 Inverse models

For the inverse models, using the monthly deformation time series from our three GPS stations and the seven surrounding PBO stations, we invert using our elastic

Green's functions for the dislocation-normal displacement required to reproduce the GPS time series displacements each month.

$$\mathbf{X} = \mathbf{G^{-1}B} \tag{2.4}$$

In this equation, X represents our inverted openings, G^{-1} is our elastic Green's functions, and B is composed of the monthly GPS displacement. For the fine grid model, which, given the large number of model parameters, would otherwise be an underdetermined problem, we use a truncated singular value decomposition to reduce the rank deficiency of the model; although a stable inverse model is obtained through this procedure, this stability comes at the expense of reduced spatial resolution in the model. This process is shown in Equations 2.5 and 2.6.

$$\mathbf{USV^T} = \mathbf{G} \tag{2.5}$$

First we decompose our G matrix from Equation 2.1 into component matrices – U and V^T are eigenvectors of the data and model space, and S contains singular values of G. We then compose our generalized inverse matrix H in Equation 2.6 by taking the pseudoinverse of our singular values, truncated by some number of values.

$$\mathbf{H} = \mathbf{U^T S^{-1} V} \tag{2.6}$$

For our fine grid models, we prefer to truncate the singular value decomposition at 8 singular values, which lies at the 'turning point' in Figure 2.8. The largest singular

values in the model are important in reducing misfit and the smaller values continually increase solution roughness and uncertainty in the estimated parameters (Harris and Segall, 1987). Above the value of 8^{th} singular value, the RMS misfit of the inverse models does not decrease. The coarse model, which only contains 3 singular values from 3 dislocations is instead inverted using a standard least-squares method. We then use the generalized inverse matrix H for G^{-1} in Equation 2.4.

We run two inverse models for each grid/dislocation model, one that includes TG03 time series data when it is available and one using only TG01 and TG02 data. To keep from having a significant number of time series to compare, we use the opening values from the inverse model with TG03 when available in conjunction with the opening values without TG03. We then compare the total volume change each month between the forward and inverse model, and also compare the modeled GPS deformation time series against the data.

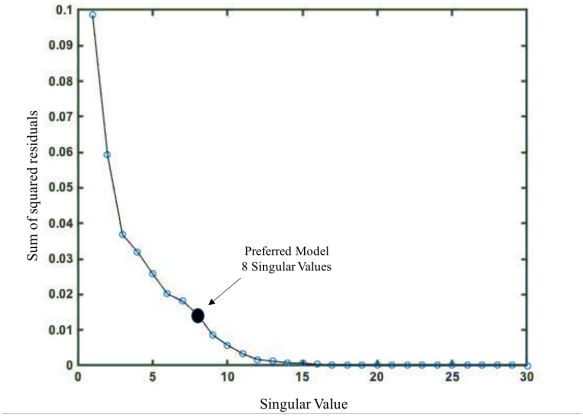

Figure 2.8: The sum of squared residuals of singular values for the fine grid inverse models. Above the value of 8^{th} singular value, the RMS misfit of the inverse models does not decrease and is thus our preferred model.

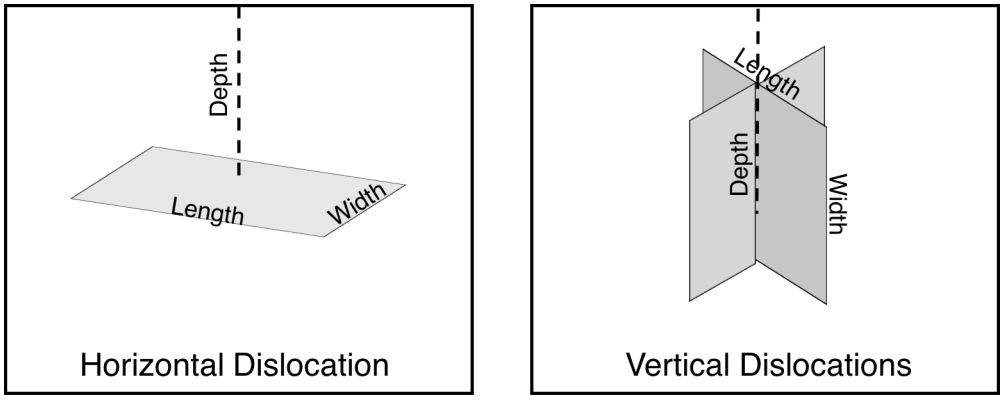

Figure 2.9: Visual representation of the horizontal and vertical dislocations used in our models, showing the definitions of length, width and depth in each case. The horizontal dislocation represents the geothermal reservoir as a horizontal opening sill, and the vertical dislocations represent two vertical conjugate dikes with opening in both perpendicular directions.

2.6 Results and discussion

2.6.1 Forward model

The observed GPS time series compared with the four model time series are shown in Figure 2.10. No model accurately and consistently reproduces all three components of the GPS time series, but the conjugate vertical dislocation models fit significantly better, with an average RMS misfit 7 times lower than the horizontal dislocation models (Figure 2.12). Both models that use horizontal dislocations produce very large subsidences – up to 200 mm at the GPS TG01 station, 400 mm at TG02 and 700 mm at TG03. The horizontal dislocations do produce a more prominent seasonal trend that is reflected in the vertical GPS components at TG01 and TG02 but the uplift produced in the model occurs 3 – 4 months prior to any uplift in the corresponding GPS time series. The models based upon conjugate vertical dislocations produced similar displacements over the 2013-2016 period and more closely reflect the change in vertical position of all GPS stations, but do not reproduce the overall uplift at TG01. When comparing the fine and coarse grid dislocation models with the vertical RMS misfit, the fine grid produces a lower misfit for all GPS stations.

The conjugate vertical dislocation models also provide an overall better fit with the horizontal components of the GPS data than the horizontal dislocation model. The average fine grid misfit is 2 – 3 times larger than both vertical dislocation models and the coarse grid misfit is 7 times larger for the north component and 3 – 4 times larger

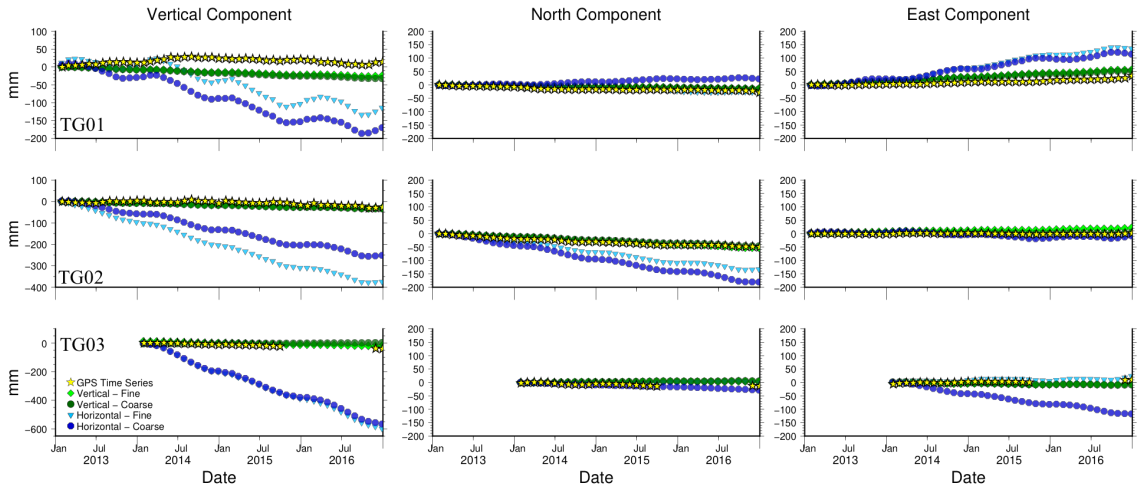

Figure 2.10: Cumulatively summed monthly model displacements for each of the four forward models compared with the GPS time series' vertical, north and east components (black). Due to the significant amount of subsidence shown in the vertical components, the horizontal components are shown on a different scale. No model can accurately predict both the horizontal and vertical components of the GPS time series but the conjugate vertical dislocations on both the coarse (dark green) and fine (light green) grids are better at predicting all components of the GPS time series than the corresponding horizontal dislocation models (dark blue and light blue, respectively).

for the east component. For the vertical dislocation models, the gridding method used does not have a significant effect on the fit, but for the horizontal dislocation models, the fine grid tends to do better. Alongside their large vertical component misfits, the horizontal dislocation models also greatly overestimate horizontal movement in both the north and east component and at all GPS stations except for the north component TG03 and the east component of TG02.

Overall, the horizontal dislocation models accounted for the highest RMS misfit values for all components except TG02 east and TG03 north, for which the vertical dislocation model RMS misfit values were only a few millimeters higher. Due to the

large differences between the RMS misfit values between the vertical and horizontal dislocation models, we prefer the vertical dislocation models and will take a closer look at them. Figure 2.11 shows the vertical component time series and horizontal vector (cumulative each year) comparison between the fine and coarse grid. The two models produce very similar time series for TG01 and TG02, but the coarse grid does not capture the continuous subsidence at TG03. Evaluating the dislocation gridding methods, the overall better fit for the vertical dislocations is from the fine grid, as the RMS misfit averaged over all components is 12 mm vs 13 mm for the coarse grid. Although the overall difference in misfit is low, it is important that the fine grid captures the subsidence at TG03. Since the coarse grid combines all of the wells in the southern portion of the field and places them on one dislocation centered north of TG03, the northern injections wells in the grid cell may have more influence.

Although the vertical dislocation models are better at reproducing the GPS time series data, there is still room for improvement. There is a possibility of fluid migration within the reservoir itself. At this time, the model only produces surface deformation from the point of each dislocation, but may be migrating to other areas of the field and producing deformation at a location farther away. No model is able to accurately capture the uplift in TG01 suggesting the northwest portion of the field

Table 2.1: RMS misfit values for all four forward models and all components compared with the GPS time-series.

Forward Model	Vertical			North			East		
	TG01	**TG02**	**TG03**	**TG01**	**TG02**	**TG03**	**TG01**	**TG02**	**TG03**
Fine Grid - Vertical	0.033	0.011	0.003	0.009	0.004	0.006	0.021	0.013	0.009
Coarse Grid - Vertical	0.035	0.013	0.014	0.007	0.007	0.008	0.017	0.003	0.011
Fine Grid - Horizontal	0.081	0.224	0.209	0.005	0.049	0.005	0.069	0.007	0.003
Coarse Grid - Horizontal	0.116	0.145	0.220	0.034	0.083	0.030	0.062	0.009	0.065

Table 2.2: Average RMS misfit values for all four forward models and all components compared with the GPS time-series.

Forward Model	**Overall**	**Vertical**	**North**	**East**
Fine Grid - Vertical	0.012	0.016	0.006	0.014
Coarse Grid - Vertical	0.013	0.021	0.007	0.010
Fine Grid - Horizontal	0.072	0.171	0.020	0.026
Coarse Grid - Horizontal	0.085	0.160	0.049	0.045

Table 2.3: RMS misfit values for all four inverse models and all components compared with the GPS time-series.

Inverse Model	Vertical			North			East		
	TG01	**TG02**	**TG03**	**TG01**	**TG02**	**TG03**	**TG01**	**TG02**	**TG03**
Fine Grid - Vertical	0.011	0.010	0.011	0.008	0.026	0.005	0.005	0.006	0.011
Coarse Grid - Vertical	0.021	0.011	0.004	0.009	0.025	0.005	0.012	0.006	0.007
Fine Grid - Horizontal	0.003	0.004	0.003	0.005	0.004	0.001	0.003	0.002	0.003
Coarse Grid - Horizontal	0.009	0.005	0.003	0.005	0.017	0.003	0.002	0.016	0.008

Table 2.4: Average RMS misfit values for all four forward models and all components compared with the GPS time-series.

Inverse Model	**Overall**	**Vertical**	**North**	**East**
Fine Grid - Vertical	0.010	0.011	0.013	0.007
Coarse Grid - Vertical	0.011	0.012	0.013	0.008
Fine Grid - Horizontal	0.003	0.003	0.003	0.003
Coarse Grid - Horizontal	0.008	0.006	0.008	0.009

may be characteristically different than the rest of the field. Another effect that is not considered but may have an influence is poroelasticity.

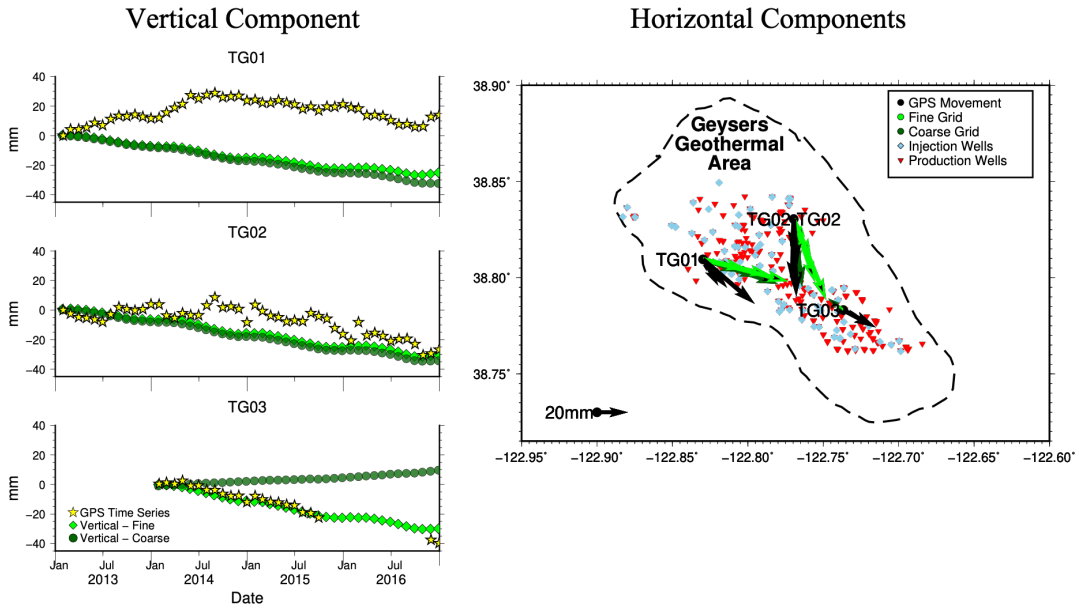

Figure 2.11: Cumulatively summed monthly model displacements each of the two conjugate vertical dislocation forward models compared with the GPS vertical time series and horizontal vectors.

2.6.2 Inverse Model

Our inverted model time series are shown in Figure 2.13 and the RMS misfits values are shown in Table 2.3 and visually represented in Figure 2.14. The inverted horizontal dislocation fine grid model reproduces the vertical component of motion very well at both TG01, TG02, and at TG03 when TG03 is included in the model, with the lowest RMS misfit (3 – 4 mm) of all models. The vertical dislocation inverse models produce overall displacements smaller in magnitude at all stations by $\sim$ 5 – 15 mm in the vertical components. Interestingly, the vertical dislocation coarse grid also produces uplift similar to the forward model (Figure 2.11) suggesting more dislocations are required to model subsidence in the southern portion of the field. Both

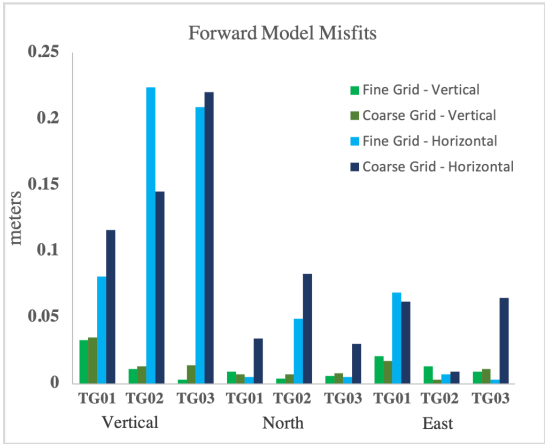

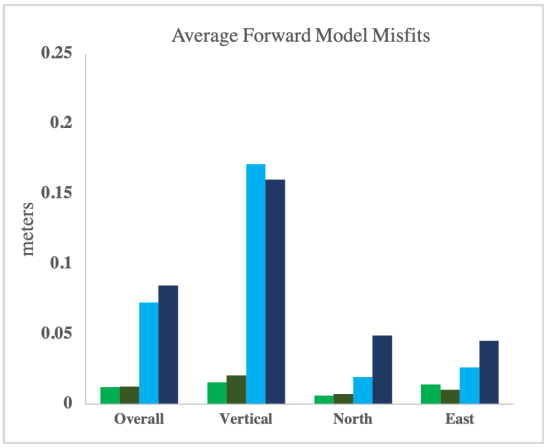

Figure 2.12: RMS misfit values (left) for all four forward models and all components compared with the GPS time-series. The vertical dislocation models provide a significantly better fit for all vertical components as the horizontal dislocation models predict a significant amount of subsidence that is not present in the data. For the horizontal components, the vertical dislocation models also provide a better fit in most instances, although the fine grid with horizontal dislocations does provide the best fit at TG01 and TG02 north and TG03 east. The average misfits for each component and overall is shown on the right. Taking an overall look at the average misfit of each model, the vertical dislocation models fit significantly better and is our preferred model.

vertical dislocation models along with the coarse grid with horizontal dislocations put little (< 20 mm) overall displacement on the north components. Only the fine grid with horizontal dislocations are able to more closely match the deformation. For the east component, the fine grid with horizontal dislocations also provides the best fit, but the other three models each have the highest misfit at one station – coarse grid - vertical at TG01, coarse grid - horizontal at TG02, and fine grid - vertical at TG03).

Overall, the inverse models have significantly lower average RMS misfit values for both horizontal dislocation inverse models than for the forward models (Figure 2.14 – note the difference in scale from Figure 2.12). These inverted horizontal dislocations also provide a better fit than the vertical dislocation models with the fine grid having the lowest misfit in all components and at all stations except TG01 east. The inverse models for the vertical dislocation models do better overall, 10 mm vs 12 mm for the fine grid and 11 mm vs 12mm for the coarse grid and is lower for both the vertical and east components, but is higher for the north component (Table 2.4).

To compare the spatial distribution of dislocation-normal displacement across the field between the forward and inverse models, we plotted their distributions in Figure 2.15. The downsampled well data has large amplitude, short wavelength variations in the spatial distribution of volume changes, both negative and positive in sign. The inverse model cannot resolve this level of variation due to the small number of GPS stations over a sparse area and instead places smaller dislocation-normal

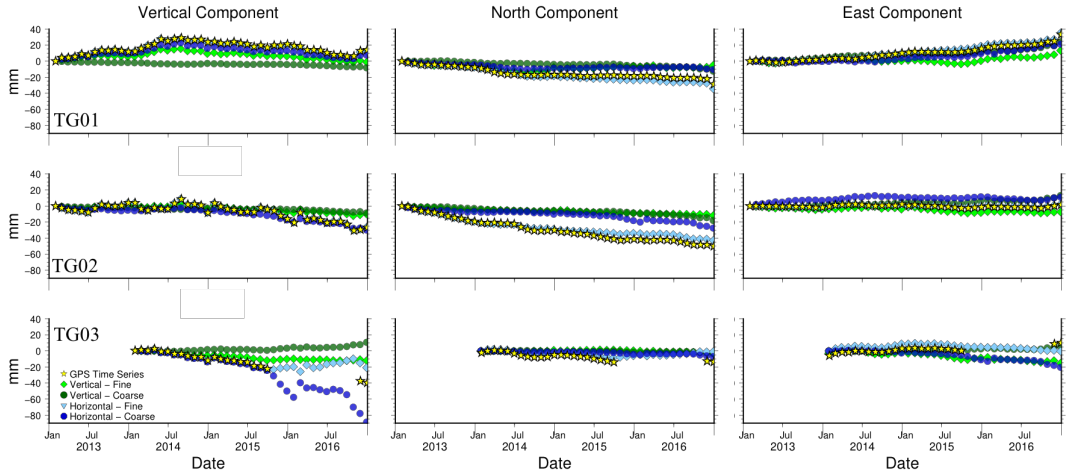

Figure 2.13: Cumulatively summed monthly model displacements for each of the four inverse models compared with the GPS time series vertical, north and east components. The horizontal dislocation models show a much better fit to the GPS displacements than with the forward models. The vertical dislocation models show improvement in the TG01 vertical component but do not appear to have a significantly better fit otherwise.

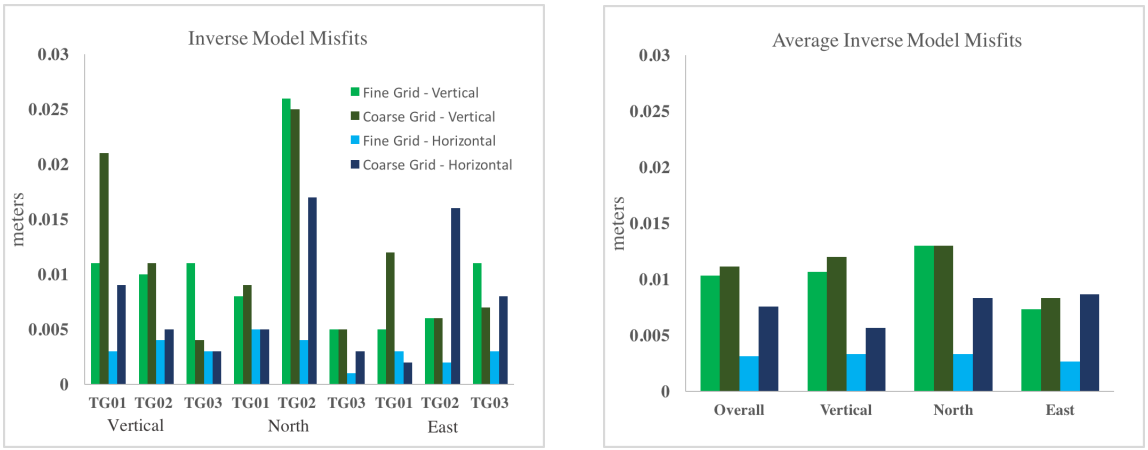

Figure 2.14: RMS misfit values (left) for all four inverse models and all components. The horizontal dislocation models provide a better fit than the vertical dislocation models with the fine grid having the lowest misfit in all components and at all stations except TG01 east. The average misfits (right) also show the horizontal dislocation models having an overall lower misfit than the vertical dislocation models. The horizontal dislocation models have significant improvement from the forward model, and the overall vertical dislocation models misfit is also lower than for the forward model.

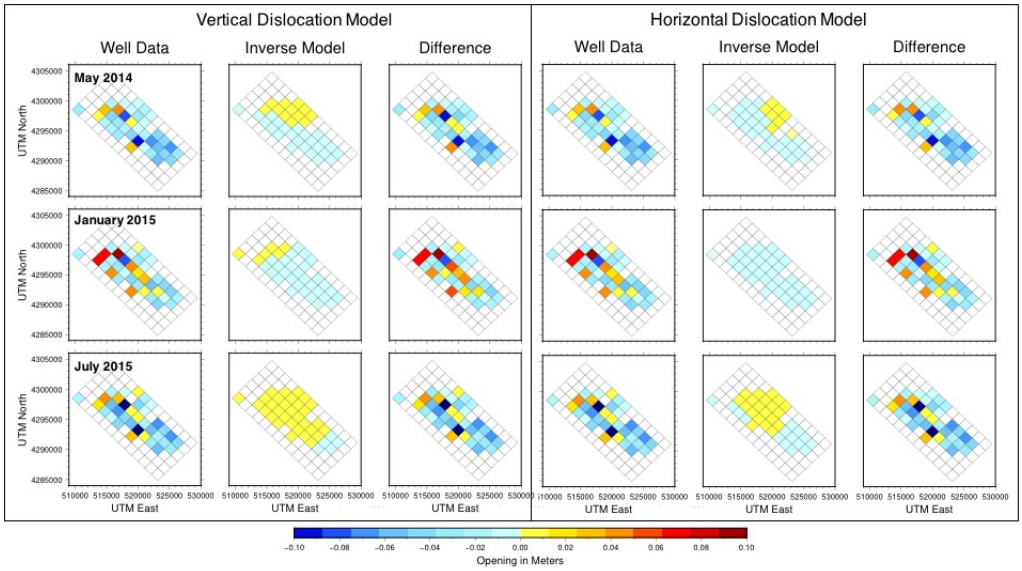

Figure 2.15: Comparison of the forward-modeled dislocation openings (dislocation-normal displacements) from well data and the openings that we invert for from GPS data for May 2014, January 2015 and July 2015. All months shown are during the period when TG03 was operating. Here we show both the fine grid model with conjugate vertical dislocations (left) and the corresponding model with horizontal dislocations (right). The low spatial resolution of the inverse models results in smaller values of opening across a wider area than the highly variable values obtained from the well data.

displacements over wider areas, suggesting that a denser deployment of GPS stations and/or a dense set of displacement measurements from a complementary technique such as InSAR would be necessary to capture some of the finer details of volume change in the field. Given the lack of resolution across the model, we find that the overall total volume change each month provides a more robust metric for comparison of the models; we compare these below.

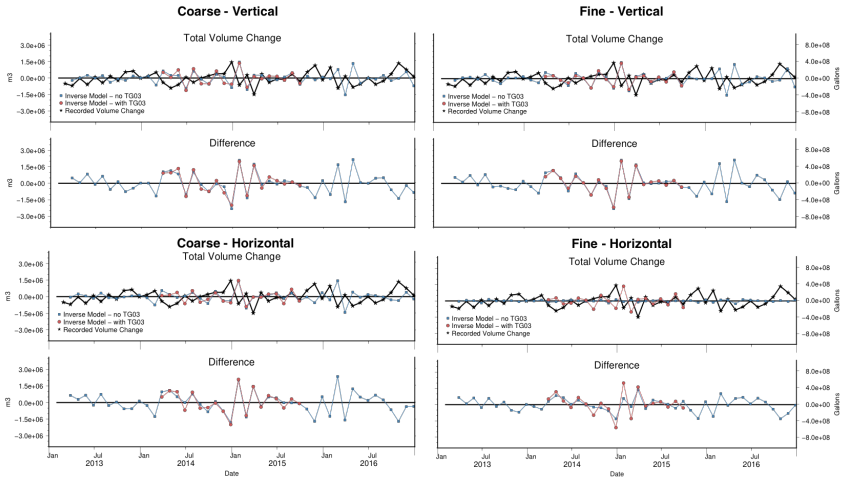

Figure 2.16: Comparison of the total volume change recorded from steam extraction and water injection in The Geysers field each month from 2013 to 2016 (black) and the total volume change in the inverse model using the GPS displacement data (with TG03: red; without TG03: blue) for all four models. All models produce similar volume changes, except for the fine grid with horizontal dislocations, which produces very small volume changes in the model that does not include TG03.

2.6.3 Total volume change

The total volume change between each month from all inverse models and from The Geysers field are shown in Figure 2.16. All models produce similar volume changes throughout all 48 months. The only model that varies significantly is the fine grid with horizontal dislocations when TG03 data are excluded, as it has very small volume changes each month. Once TG03 is introduced in the model, it produces similar volume changes.

For all inverse models, there are periods of several months where the estimated volume changes are in phase with the reported volume change within The Geysers field (Figure 2.17), and periods where they are out of phase by one month (with the

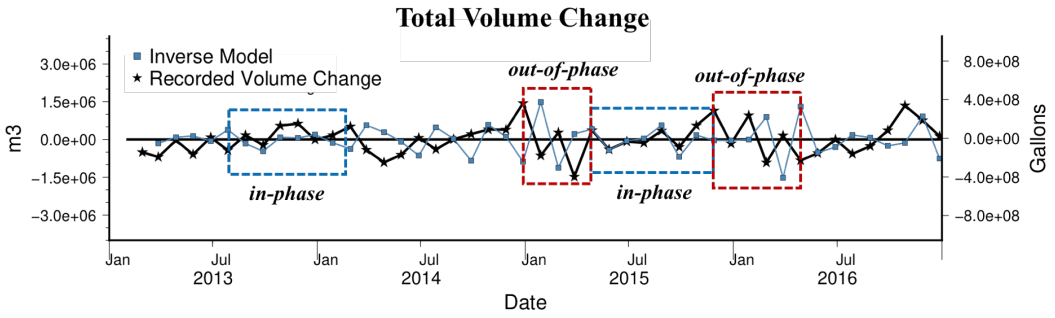

Figure 2.17: Comparison of the total volume change recorded from steam extraction and water injection in The Geysers field each month from 2013 to 2016 (black) and the total volume change in the inverse model using the GPS displacement data. Notable times when a phase shift occurs are shown (red boxes – January - April 2015, and January - April 2016) and when the model is in phase (blue box - August 2013 - February 2014 and May - November 2015).

reported values showing a peak one month before the inverse modeled values). These out-of-phase periods are marked by large amplitude differences between the reported and modeled volume time series, particularly notable between January and April in 2015 and 2016 in all inverse models (Figure 2.18); in-phase periods, in contrast, show smaller differences, for example between May and October 2015 (Figure 2.18). These out-of-phase periods are temporally correlated with the periods of the highest injection across the field (Figure 2.18). This coincidence in time with peak injection and the one-month phase lag of the models with respect to the total volume change may indicate a delayed surface deformation response to large changes in volume injected into the reservoir, possibly related to the finite permeability of the rocks of the geothermal reservoir.

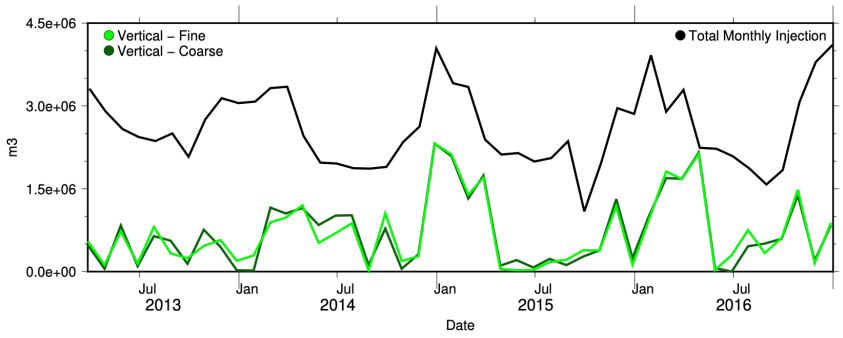

Figure 2.18: Difference between total injected volume each month and the absolute difference in the total inverted volumes from the two vertical dislocation models. There is a larger absolute difference following periods of high injection/reduced overall extraction.

2.6.4 Investigating time lag

By comparing the difference between the inverted volume change and recorded volume change in the field, we identified a possible time lag between injection and surface deformation. To see if there is a correlation between fit of the data and delayed injection, we shifted our conjugate vertical dislocation forward model (injection only) time-series forward in time by 1 to 8 months. We then calculated the RMS misfit (Figure 2.19 between the GPS and model time series to see if an improvement in fit occurred. Although the vertical and east component sees reduction of misfit of up to 56%, the north component and one model in the vertical component sees misfit increased up to 214%. This suggests that the time lag seen in the total volume may be restricted to periods of high injection as seen by the in and out of phase periods in Figure 2.17.

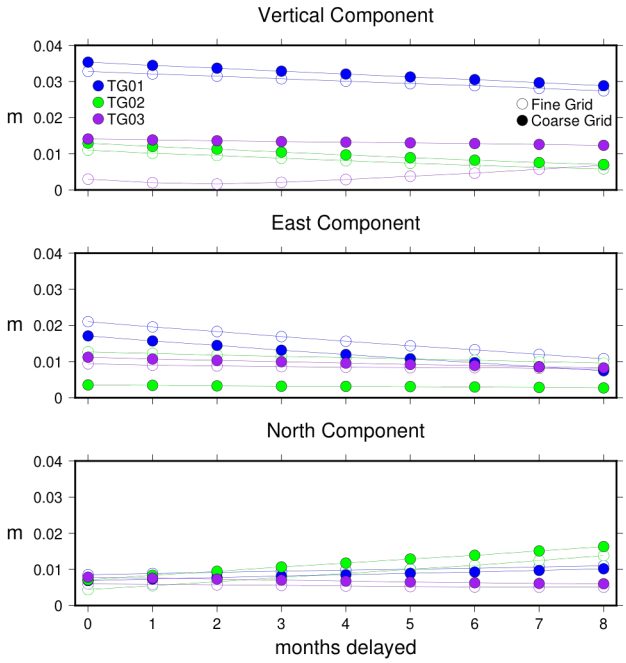

Figure 2.19: RMS misfit values for each GPS, component, and downsampled grid starting with the forward model (0 months delayed) and going to injection delay of 8 months. Delaying injection from 1 -8 months did not consistently change the misfit between the model time series and the GPS time series. In the vertical and east component, the reduction in misfit was up to 50%, but in the north component, the misfit increased up to 200%.

2.7 Conclusions

In our first attempt to interpret GPS time series data from The Geysers, we use downsampled monthly steam extraction and water/wastewater injection volumes from The Geysers field and input them into a rectangular elastic dislocation model within an isotropic elastic half space (e.g. Okada 1985). Our four forward models used in this study fail to reproduce the multi-annual trends of our GPS time series data. Possible explanations for why they do not include fluid migration within the reservoir, poroelastic deformation and/or changes in the compressibility of the reservoir. Both models with horizontal dislocations produce a significantly higher amount of vertical deformation than is observed. The average RMS misfit for the conjugate vertical dislocation models is 7 times smaller than for the horizontal dislocation models and is the preferred means of modeling the reservoir. Since The Geysers have evidence of vertical fracture networks, the horizontal dislocation models are not representative of The Geysers and are placing majority of surface deformation in the vertical direction.

Using the GPS time series data, we next invert for the opening (dislocation-normal displacement) required at each model dislocation, and therefore the volume changes in the reservoir, that best reproduce the time series data. Since our sparse data coverage provides low spatial resolution for our model, we summed volume changes for the whole model domain each month to compare those estimated from inverse models to reported well data. The total volume change was similar between all four inverse models which shows the robustness of our inverse model. There were periods

of time that were in and out of phase with the recorded total volume changes in the field. In the latter cases, the peaks in volume changes estimated in our models lag those from the well data by 1 month. The periods of time when the total volume changes are out of phase occur during periods of high injection volumes, in the winter and early spring. This may indicate a time lag between injection into the wells and the resulting surface deformation that is due to the finite permeability of the reservoir rocks. To investigate a time lag, we delayed our forward model injection time series by 1-8 months, but were unable to find an overall direct correlation. The time lag may be restricted to periods of high injection.

2.8 Future Work

Simplistic models by themselves are not able to fully explain the deformation in The Geysers geothermal field. The results suggest that geothermal reservoirs have a degree of complexity that cannot be explained with instantaneous surface deformation or even a lagged deformation signal. The models we used calculate surface deformation due to dislocations at depth within an elastic half-space. Whether fluid migration plays a role, how far is migrates, in which directions, and whether it would migrate consistently over time within The Geysers reservoir remains unknown, but should be researched in the future. Another complexity that could be added to the simple models is a poroelastic component, modeling the pore pressure changes within the reservoir. If fluid migration is considered, the pore pressure changes would be

induced or spread over some distance from the well location. Since The Geysers has been in operation for about sixty years, one must also consider the long-term effects of permanent porosity reduction (compaction of pore-space) at The Geysers, including how the period of over-production affected the reservoir in the 1980s and whether it can return to its original state. Previous studies suggest that thermoelastic effects do not primarily control surface deformation (Mossop et al., 1997; Vasco et al., 2013; Rutqvist et al., 2015), but could also be incorporated into a model.

Our three GPS stations in the Geysers have provided us with a unique dataset that includes daily movement, but are limited in spatial coverage. Campaign GPS, although more limited in temporal resolution, may help to see the long term deformation pattern in and around The Geysers. More continuous GPS could be installed in The Geysers to get a better spatial resolution of deformation. GPS data can also be used jointly with InSAR or LiDAR. The shortening of InSAR satellite fly-by time intervals in recent satellite missions like Sentinel-1 provides an opportunity to see wide spatiotemporal deformation at The Geysers field. To my knowledge, LIDAR has not been using to study deformation in geothermal fields but could be used to do in the future. Previously flown LiDAR for Lake and Sonoma counties have a small overlap directly over The Geysers field and could potentially be differenced for surface displacement. The method to do this is known as 'Iterative Closest Point' and aligns 3-dimensional points from two datasets using rigid body rotation. For now, the

previous datasets that overlap The Geysers is the only option to test if it is capable of measuring surface deformation in the field until future LiDAR surveys are flown.

Chapter 3

The Geysers $M_w5.0$ earthquake: observations and models

3.1 Introduction

The Geysers geothermal area is the most seismically active area in California. Prior to the start of geothermal production, there was little seismicity (Trugman et al., 2016). At 8:41am local time on December 14th, 2016, the geothermal area experienced a $M_w5.0$ earthquake, located in the northwest portion of the field. To this date, this earthquake is the largest earthquake that has ever been recorded in The Geysers reservoir area. Since production began in the 1960s, there have been 31 $M_w > 4.0$ earthquakes (Figure 3.1), with the first $M_w4.0$ earthquake occurring in 1982. Of these larger earthquakes, there have only been five $M_w4.5$ and above

earthquakes, with the first M_w4.5 event in 1992, a M_w4.6 event in 2004, M_w4.6 and M_w4.7 events in 2006, M_w4.5 event in 2014, and the M_w5.0 event in 2016.

Earthquakes in The Geysers typically occur at shallow depths (<6 km) and with $M_w < 3.0$. The M_w5.0 earthquake had a very shallow depth (1.5 km), according to estimates made by the United States Geological Survey (USGS). Shallow depths suggest a connection between the earthquake and the production and injection activities within the field, as the depth of this earthquake is similar to the depths of the injection wells in the field. Earthquakes in The Geysers have been shown to deviate from normal California seismicity with moment tensors of $M_w > 3.0$ earthquakes showing large volume-compensated linear vector dipole (CLVD) components accompanying normal and strike-slip events (Boyd et al., 2015).

In this chapter, I will present our recorded co-seismic displacements in our continuous GPS time series in The Geysers field as well as at one Plate Boundary Observatory (PBO) GPS station that lies northwest of the field, close to where the earthquake occurred. Given both the co-seismic displacements and the earthquakes' shallow depths, we processed both ascending and descending interferograms using Sentinel-1 data for multiple time periods before and after the earthquake. I will present results of forward and inverse modeling, using the Okada elastic dislocation model (Okada, 1985) and the Okinv modeling code (Clarke et al., 1997; Wright et al., 1999) to determine the best-fit earthquake source parameters.

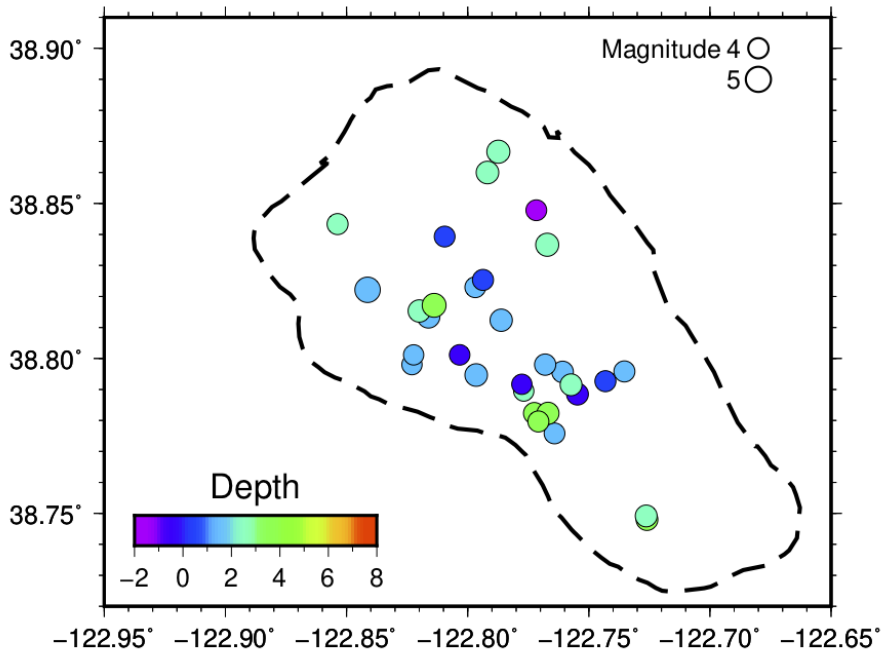

Figure 3.1: This map shows the 31 $M_w > 4$ earthquakes in The Geysers geothermal area since production began. All of these earthquakes have shallow depths of less than 5 km, consistent with depths of the geothermal reservoir.

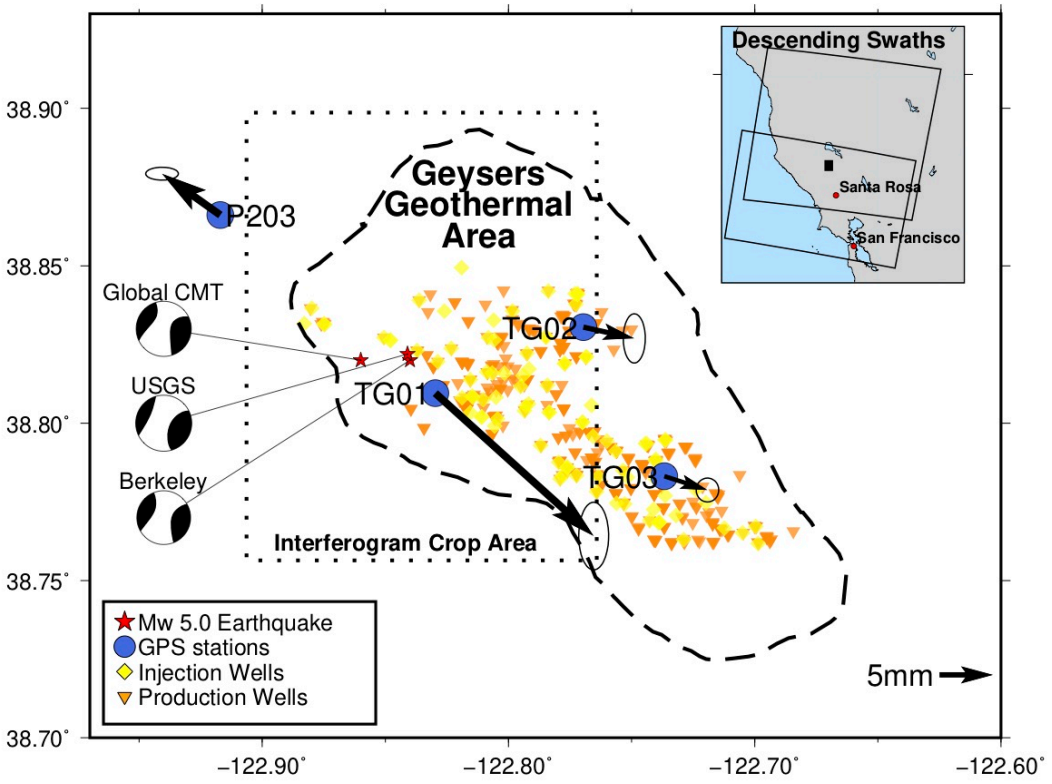

Figure 3.2: Map of The Geysers Geothermal area showing the coseismic GPS displacements for the December 14^{th}, 2016 M_w5.0 earthquake as horizontal vectors for each continuous GPS station in The Geysers (TG01, TG02, TG03) and for the PBO station closest to the field (P203). The earthquakes' locations (red stars) and moment tensor solutions provided by the USGS, Global CMT, and Berkeley Moment Tensor Project catalogs are shown to the left. The map inset shows the two descending interferogram frames used to create December 13th–December 19th interferogram (Path 115, Frame 465 and 461, respectively). The dotted box shows our cropped interferogram area that we use to compare with our forward and inverse models.

3.2 Moment tensor solutions

Moment tensor solutions from three sources are shown in Figure 3.2 and their nodal planes parameters are shown in Table 3.1. The three moment tensor solutions – USGS (https://earthquake.usgs.gov/earthquakes/), Global Centroid Moment Tensor

Table 3.1: Nodal plane parameters provided for The Geysers M_w5.0 earthquake from The Global Centroid Moment Tensor Catalog, Berkeley Moment Tensor Catalog and from the USGS catalog

	Nodal Plane 1		
	Strike	**Dip**	**Rake**
USGS	250°	76°	6°
Global CMT	247°	65°	-12°
Berkeley	244°	75°	-7°
	Nodal Plane 2		
USGS	336°	84°	-166°
Global CMT	342°	79°	-155°
Berkeley	335°	83°	-165°

Catalog (https://www.globalcmt.org/) (Dziewonski et al., 1981; Ekström et al., 2012), and the Berkeley Moment Tensor Project (http://seismo.berkeley.edu/mt/) – all show similar moment tensor solutions. The first nodal plane has a WSW strike 244 – 250°, with dips from 65 – 75°, and a rake from -12 – 6°. The second nodal plane has a NNW strike of 335 – 342°, with dips of 79 – 84°, and rakes of -155 – -166°. All solutions had a depth of 1.5 km. The USGS and Global CMT catalogs reported a magnitude of 5.1 and the Berkeley catalog reported a magnitude of 5.0. The steep dips and close to strike-parallel rakes are indicative of strike-slip motion, though the moment tensors also suggest a component of non-double couple motion. The USGS reported a significant (74%) non-double couple component, indicating the earthquake may have a non-shear component to it, consistent with other large CLVD earthquakes in The Geysers (Boyd et al., 2015).

3.3 Co-seismic GPS displacements

In December 2012 and December 2013, Gareth Funning and Michael Floyd installed three continuous GPS stations in The Geysers geothermal area. These installments were a more permanent continuation of previous campaign GPS and leveling surveys to monitor surface deformation at The Geysers due to production activities. The Geysers geothermal area has a high concentration of seismic activity, with the majority of earthquakes being too small to record surface displacements. Large shallow earthquakes, like the 2016 M_w5.0 event, are capable of being captured in GPS time series. Our GPS stations, TG01, TG02, and TG03, and P203, a station that is part of the Plate Boundary Observatory (PBO) network, just north of The Geysers area, recorded coseismic displacements in their horizontal components. The horizontal displacement vectors are shown in Figure 3.2 and their displacement values are shown in Table 3.2.

The three Geysers GPS stations, TG01, TG02, and TG03, all recorded horizontal southeast displacements during the earthquake. TG01, which is the closest GPS station to the earthquake's epicenter, recorded the most displacement, ∼20 mm SE. TG02 and TG03 recorded displacements of ∼5 mm and ∼4 mm SE respectively. The PBO station, P203, recorded the second largest movement during the earthquake, moving ∼7 mm in an overall northwest direction.

Table 3.2: Coseismic GPS displacements for our three continuous GPS stations and the nearest Plate Boundary Observatory GPS station, in millimeters, for all components from The Geysers M_w5.0 earthquake. Negative values indicate displacement in the reverse direction (i.e. west or south).

GPS	East	North
TG01	14.8 ± 0.7 mm	-13.3 ± 1.5 mm
TG02	4.8 ± 0.5 mm	-1.1 ± 1.1 mm
TG03	4.0 ± 0.5 mm	-1.3 ± 0.5 mm
P203	-5.4 ± 0.7 mm	3.9 ± 0.3 mm

3.4 InSAR observation of The Geysers earthquake

Interferometric Synthetic Aperture Radar (InSAR) is a geodetic technique commonly used to map deformation from large earthquakes on the continents. The most important part of recording these earthquakes with InSAR is to have high correlation between the 'before' image and the 'after' image. Correlation, the quality of the InSAR signal, can be affected by many factors that may be present during time of each acquisition. Long time-spans between acquisitions, or acquisitions in different seasons can decrease correlation due to human induced changes in the land surface (infrastructure, agriculture, etc.), or natural vegetation seasonal changes. The angle of illumination effects the radars return signal during each acquisition and can vary based on the satellites orbital position. We call the distance between the satellite in the first acquisition and the second acquisition its perpendicular baseline. The larger the difference, the higher the chance of low correlation between to the two images. In addition, differences in atmospheric conditions present at the time of acquisition can also add noise to the data, typically due to changes in tropospheric water vapor or

charged particles in the ionosphere. Specifically related to The Geysers geothermal area is its location in a highly vegetated, mountainous region. This makes detection of small earthquakes in The Geysers more difficult.

Earthquake depth and magnitude are two primary factors that determine whether deformation is detected. Shallow (<10 km depth) earthquakes with magnitudes greater than 5.5 are often detected (Funning and Garcia, 2018). In a study using 96 M_w4.5 – M_w5.5 events in the Zagros mountains in southern Iran, only 4 events, all with depths of <5 km were detected (Lohman and Simons, 2005), highlighting the lower range of detectability. The 2016 Geysers M_w5.0 earthquake occurred at a significantly shallow depth of 1.5 km making its detection feasible. For this earthquake, we processed both descending and ascending interferograms from the Sentinel-1 satellites using the software package, ISCE (InSAR Scientific Computing Environment) (Rosen et al., 2012). We processed interferograms with various dates ranging from early November through mid-January.

We were only able to detect the earthquake in one descending interferogram, which had acquisition dates closest to the earthquake on December 14th, 2016. The descending interferogram acquisitions were one day before the earthquake on December 13th, 2016 and 4 days after the earthquake on December 19th, 2016, a total 6-day timespan and 35 m perpendicular baseline. Luckily, acquisitions for this area switched to a 6-day interval between the two Sentinel-1 satellites in December 2016 which was previously 24-days. Prior to the acquisition on December 13th, the previous ac-

quisitions occurred on November 19th (descending) and November 20th (ascending). There was an ascending acquisition on the day of the M_w5.0 earthquake that was acquired post-earthquake, but did not correlate well with the previous acquisition dates. November 19th experienced the highest (to this day) recorded rainfall for that day with 2.63 in of rain recorded and November 20th experienced 0.3 in of rain. The high amounts of water vapor present during these rainy days may have overprinted the small earthquake signal.

The full descending interferogram from December 13th, 2016 – December 19th, 2016 is shown in Figure 3.3. The signal is small (9 km × 4.5 km), as expected for a M_w5.0 earthquake, but is noticeable ∼15 km south of Clearlake. To isolate the earthquake for use in forward and inverse model calculations, we cropped the interferogram to the black box shown in Figure 3.3 and a closer view of The Geysers area, GPS stations and earthquake location from the USGS in Figure 3.2. The cropped interferogram includes the closest GPS station just southeast of the earthquake, TG01 and our GPS station TG02 due east of the earthquake.

3.5 Atmospheric correction

When cropping the interferogram to the location just around the earthquake signal, it appeared as though the deformation was overprinted by an atmospheric signal (Figure 3.4), which may be masking or obscuring the earthquake deformation sig-

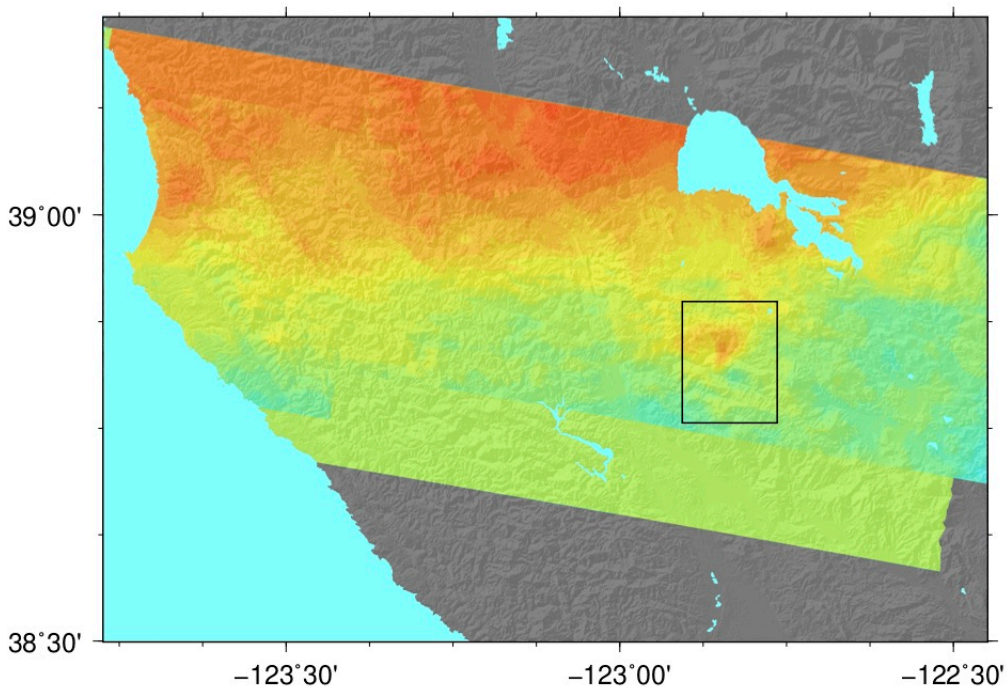

Figure 3.3: Interferogram from descending track (Path 115 - Frame 465 and 461) spanning December 13th, 2016 – December 19th, 2016. Deformation due to the Geysers earthquake is indicated by the black box.

nal. Topographic features, most notably steep elevation changes, affect the density of water vapor in the troposphere and since The Geysers is located in a mountainous region, these water vapor signals will show up in interferograms. We wanted to remove this atmospheric signal from our cropped interferogram to be able to more accurately model the deformation signal. To remove the atmosphere, we masked out the cropped area containing the earthquake from the interferogram and from the digital elevation model (DEM). We then solved simultaneously for the linear scaling between elevation and phase in the rest of the cropped interferogram and for the E-W and N-S tilts that minimized phase in the area surrounding the earthquake. The predicted atmospheric

signal is shown in Figure 3.4. We then removed this predicted atmospheric noise signal from the cropped interferogram, revealing a more clear earthquake deformation pattern (Figure 3.4).

The final cropped interferogram with the earthquake epicenter and nearest GPS station, TG01, is shown in figure 3.4. The earthquake signal is more clearly visible than before the atmospheric correction. The total line-of-sight displacement is on the order of ∼3 cm. This deformation pattern is consistent with the co-seismic deformation from the continuous GPS stations in the area. The interferogram is also consistent with the deformation pattern of forward-modeled strike-slip earthquakes (Funning and Garcia, 2018).

3.6 Modeling The Geysers earthquake

To better understand the fault parameters of The Geysers earthquake, we produce forward-modeled interferograms modeling slip on a fault plane, using the Okada elastic dislocation formulation (Okada, 1985). We began by using the fault parameters from the moment tensor solutions provided in Table 3.1 to identify the best-fit nodal plane. The location, depth, width and length of the fault were varied manually to match the pattern of deformation between the model and the interferogram. The depth to fault centroid and fault width were constrained to include the moment tensor depths of ∼1.5 km. The model parameters were adjusted such that the output

magnitude stayed within the range 5.0 ± 0.1. Figure 3.5 shows both models, and the parameters that produced the best-fitting overall patterns of deformation. Both nodal planes produce deformation patterns that are generally similar in appearance to the descending interferogram and with corresponding magnitude of deformation. From this forward modeling, we cannot distinguish which nodal plane is the fault plane.

We also ran a preliminary inverse model using the non-linear inverse dislocation modeling code, okinv (Wright et al., 1999). Before running the inversion algorithm, we needed to downsample the data to only the most important data points. Although we applied an atmospheric correction to the interferogram, we do not wish to model any remaining atmosphere or effects not related to the earthquake. To do this, we use quadtree decomposition (Jónsson et al., 2002) to identify the most significant data points within the cropped interferogram. Quadtree decomposition works by focusing the sampling of data points in the image to areas of high variance. This method is particularly useful in modeling interferograms because we want the most data points to be where the deformation is the greatest. After reducing the number of data points, we solve simultaneously for all fault parameters including strike, dip, rake, dimensions, depth, and location. We constrain parameters to be within reasonable bounds using seismological estimates of the strike, dip, rake rake and depth of the earthquake. The model with the lowest misfit is shown in Figure 3.6 and output parameters are shown in Table 3.3. The output from the inverse model is closest to

Parameter	Value
Strike	338°
Dip	55°
Rake	-160°
Slip	1.25 m
Scarp Length	2.5 km
Depth	2.0 km
Moment Magnitude	4.9

Table 3.3: Inverse model output parameters for best-fitting fault. Fault plane is similar to the 2^{nd} nodal plane from the three seismological sources shown in Table 3.1.

the NNW striking nodal planes. The only significant variation from the nodal planes is the dip, for which the inverse model suggests a more shallow-dipping value of 55°.

3.7 Conclusions

The M_w5.0 earthquake that occurred at 8:41 am local time on December 14^{th}, 2016 in The Geysers is currently the largest recorded earthquake in the geothermal field. The shallow depth (1.5 km) of the earthquake means that it is a rare earthquake capable of producing geodetically-measurable ground surface deformation. Our nearby continuous GPS stations and one PBO station recorded co-seismic displacements upwards of 1.5 cm. We were able to identify earthquake deformation in the shortest time span (6–day) descending interferogram available from the Sentinel-1 satellite data. Tropospheric noise likely overprinted the small deformation signal in other interferograms. To remove any atmospheric effects in the 6–day descending

interferogram, we solved for the linear scaling between elevation and phase in the area surrounding the earthquake and removed this signal to produce our final interferogram. This interferogram showed a total line-of-sight displacement of about 3 cm and was consistent with the recorded co-seismic deformation from the continuous GPS station data.

To identify fault parameters of the earthquake, we modeled slip on a fault plane using the nodal planes provided three seismological catalogs – USGS, Global CMT, and Berkeley – and observed the pattern of deformation and calculated the residuals between the interferogram and the models. From this forward modeling, both nodal planes produced a consistent spatial pattern with the recorded displacement. Our inverse modeling closely matched the NNE-striking nodal plane, with similar strike and rake but with a more shallow dip (55° vs 79 – 84°). Future work could be done to more accurately assess The Geysers earthquake, including more detailed slip modeling, joint InSAR-GPS modeling, and comparison with precise seismic aftershock locations.

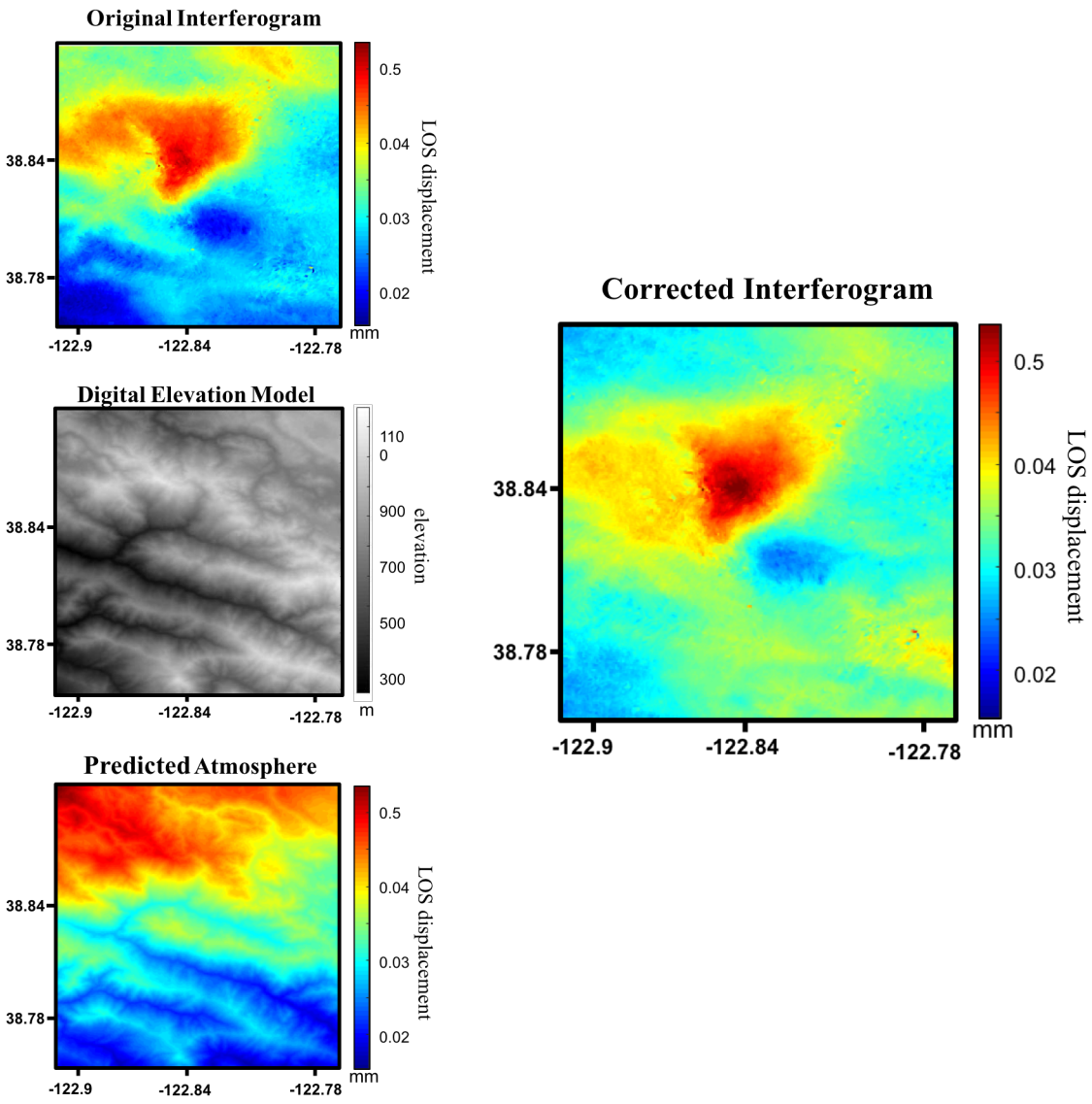

Figure 3.4: Here we show our interferogram atmosphere correction process. The original interferogram (top left) shows an atmospheric signal overlaying the earthquake signal. By using the E-W and N-S tilts (seen in overall swath image of Figure 3.3) and the DEM (middle left), we solved simultaneously for linear scaling between the tilts and the elevation and phase. From these two processes, we predicted the atmospheric effects that would overprint the earthquake signal (bottom left). The predicted atmosphere is then subtracted from the original interferogram, resulting in our corrected interferogram (right). The result enhances the ability to see the earthquakes displacement. The final cropped descending interferogram for December 13th–December 19th, 2016 with the atmospheric correction shows $\sim$ 3 cm of movement.

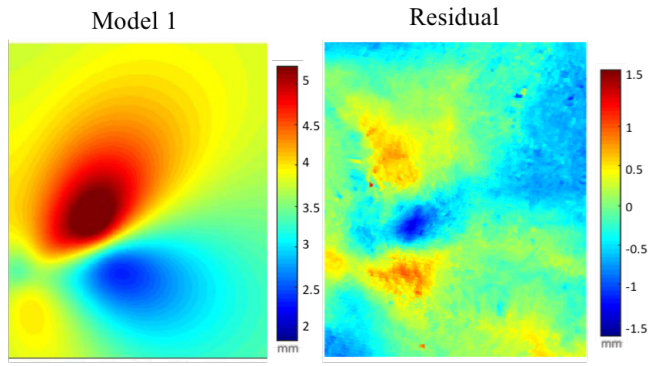

Fault Plane 1	
Strike	245
Dip	75
Rake	1
Slip	0.22 m
Length	2.5 km
Width	3.5 km
Depth (centroid)	2.35
Mw	5.2

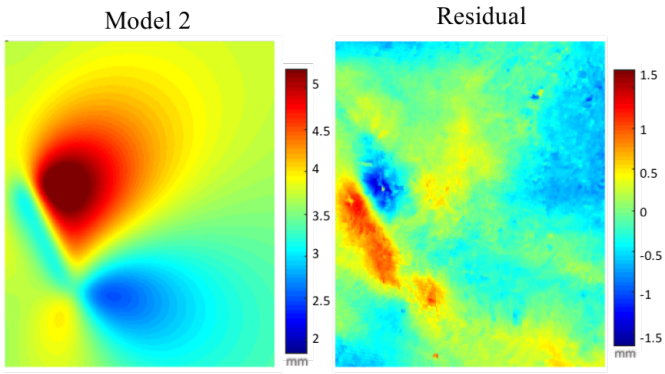

Fault Plane 2	
Strike	337
Dip	85
Rake	-162
Slip	0.2 m
Length	3.2 km
Width	3.0 km
Depth (centroid)	2.0 km
Mw	5.14

Figure 3.5: Two best-fit models of surface deformation modeling slip on a fault using the Okada elastic dislocation code (Okada, 1985). The models were based on the USGS preliminary nodal planes for the earthquake (Table 3.1) and altered to find the lowest residual (misfit) to the corrected interferogram (Figure 3.4). The resulting model parameters are shown on the right.

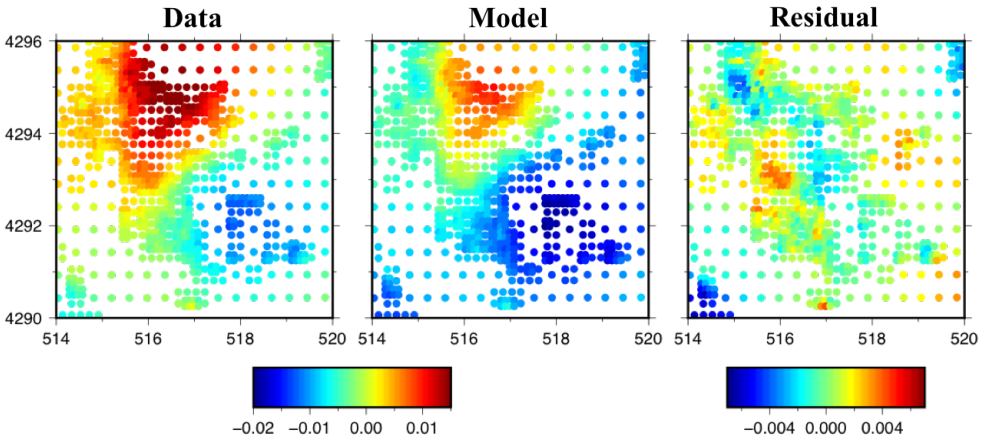

Figure 3.6: Best-fitting preliminary inverse model using a non-linear inversion algorithm (Wright et al., 1999) to solve for fault parameters. Best-fitting parameters are shown in Table 3.3

Bibliography

Ali, S., J. Akerley, E. Baluyut, M. Cardiff, N. Davatzes, K. Feigl, W. Foxall, D. Fratta, R. Mellors, P. Spielman, et al. (2016). Time-series analysis of surface deformation at brady hot springs geothermal field (nevada) using interferometric synthetic aperture radar. *Geothermics 61*, 114–120.

Allis, R. (1982). Mechanism of induced seismicity at the geysers geothermal reservoir, california. *Geophysical research letters 9*(6), 629–632.

Atwater, T. (1970). Implications of plate tectonics for the cenozoic tectonic evolution of western north america. *Geological Society of America Bulletin 81*(12), 3513–3536.

Bailey, E. H., W. P. Irwin, and D. L. Jones (1964). Franciscan and related rocks, and their significance in the geology of western california. Technical report, California Division of Mines and Geology.

Beall, J. J., M. C. Wright, A. Pingol, and P. Atkinson (2010). Effect of high rate injection on seismicity in the geysers. *Geothermal Resources Council Transactions 34*, 1203–1208.

Blewitt, G. (2007). *GPS and space-based geodetic methods*. Elsevier.

Bowen, R. G. (1973). Environmental impact of geothermal development. *In: Geothermal Energy–Resources, Production, Stimulation 1*, 197–215.

Boyd, O. S., D. S. Dreger, V. H. Lai, and R. Gritto (2015). A systematic analysis of seismic moment tensor at the geysers geothermal field, california. *Bulletin of the Seismological Society of America 105*(6), 2969–2986.

Boyle, K. and M. Zoback (2013). Stress and fracture orientation in the northwest geysers geothermal field. In *Proceedings of the 38th workshop on geothermal reservoir engineering, Stanford University, Stanford, California*.

Brophy, P., M. Lippmann, P. F. Dobson, and B. Poux (2010). The geysers geothermal field update 1990/2010. Technical report, Lawrence Berkeley National Lab.(LBNL), Berkeley, CA (United States).

California Department of Conservation, Division of Oil, Gas, and Geothermal Resources (2017, 2). *Oil, Gas, and Geothermal*. California Department of Conservation, Division of Oil, Gas, and Geothermal Resources.

Calpine (2018). The geysers: A very special place".

Capetti, G. (2006, 2). How egs is investigated in the case of the larderello geothermal field. ENGINE Launching Conference.

Carnec, C. and H. Fabriol (1999). Monitoring and modeling land subsidence at the cerro prieto geothermal field, baja california, mexico, using sar interferometry. *Geophysical Research Letters 26*(9), 1211–1214.

Chapman, R. H. (1975). Geophysical study of the clear lake region, california. Technical report, California Division of Mines and Geology, Sacramento, CA.

Clarke, P., D. Paradissis, P. Briole, P. England, B. Parsons, H. Billiris, G. Veis, and J.-C. Ruegg (1997). Geodetic investigation of the 13 may 1995 kozani-grevena (greece) earthquake. *Geophysical Research Letters 24*(6), 707–710.

Denlinger, R. and C. Bufe (1980). Seismicity induced by steam production at the geysers steam field in northern california. *Eos Trans. AGU 61*(46), 1051.

Dong, D., P. Fang, Y. Bock, M. Cheng, and S. Miyazaki (2002). Anatomy of apparent seasonal variations from gps-derived site position time series. *Journal of Geophysical Research: Solid Earth 107*(B4), ETG–9.

Dziewonski, A., T.-A. Chou, and J. Woodhouse (1981). Determination of earthquake source parameters from waveform data for studies of global and regional seismicity. *Journal of Geophysical Research: Solid Earth 86*(B4), 2825–2852.

Eberhart-Phillips, D. and D. H. Oppenheimer (1984). Induced seismicity in the geysers geothermal area, california. *Journal of Geophysical Research: Solid Earth 89*(B2), 1191–1207.

Ekström, G., M. Nettles, and A. Dziewoński (2012). The global cmt project 2004–2010: Centroid-moment tensors for 13,017 earthquakes. *Physics of the Earth and Planetary Interiors 200*, 1–9.

Eneva, M., G. Falorni, W. Teplow, J. Morgan, G. Rhodes, and D. Adams (2011). Surface deformation at the san emidio geothermal field, nevada, from satellite radar interferometry. *Geothermal Resources Council Transactions 35*, 1647–1653.

Fialko, Y. and M. Simons (2000). Deformation and seismicity in the coso geothermal area, inyo county, california: Observations and modeling using satellite radar interferometry. *Journal of Geophysical Research: Solid Earth 105*(B9), 21781–21793.

Floyd, M. A. and G. J. Funning (2013). Continuation of survey gps measurements and installation of continuous gps sites at the geysers, california, for geothermal deformation monitoring. *Transactions - Geothermal Resources Council 37*, 895–898.

Foulger, G. R., M. P. Wilson, J. G. Gluyas, B. R. Julian, and R. J. Davies (2018). Global review of human-induced earthquakes. *Earth-Science Reviews 178*, 438–514.

Funning, G. J. and A. Garcia (2018). A systematic study of earthquake detectability using sentinel-1 interferometric wide-swath data. *Geophysical Journal International 216*(1), 332–349.

Garcia, J., C. Hartline, M. Walters, M. Wright, J. Rutqvist, P. F. Dobson, and P. Jeanne (2016). The northwest geysers egs demonstration project, california: Part 1: characterization and reservoir response to injection. *Geothermics 63*, 97–119.

Garcia, J., M. Walters, J. Beall, C. Hartline, A. Pingol, S. Pistone, and M. Wright (2012). Overview of the northwest geysers egs demonstration project. *Proceedings of the Thirty-Seventh Workshop on Geothermal Reservoir Engineering 37*, 1–11.

Gettings, P., R. Harris, R. Allis, and D. Chapman (2002). Gravity signals at the geysers geothermal system. *In Proceeedings, Twenty-Seventh Workshop on Geothermal Reservoir Engineering 27*, 425–430.

Gipe, P. (1990, 2). Losing steam at the geysers. *Independent Energy; (United States) 20:2*.

Goyal, K.P., P. A. (2007). Geysers performance update through 2006. *Geothermal Resources Council Transactions 31 31*, 435–439.

GPS.gov (2019, 1). Space segment. Accessed 2019-01-28.

Gritto, R., S.-H. Yoo, and S. P. Jarpe (2013). Three-dimensional seismic tomography at the geysers geothermal field, ca, usa. In *Proceedings, 35th Workshop on Geothermal Reservoir Engineering, Stanford Univ., Stanford, Calif.*

Gunasekera, R. C., G. Foulger, and B. Julian (2003). Reservoir depletion at the geysers geothermal area, california, shown by four-dimensional seismic tomography. *Journal of Geophysical Research: Solid Earth 108*(B3), 1–11.

Harris, R. A. and P. Segall (1987). Detection of a locked zone at depth on the parkfield, california, segment of the san andreas fault. *Journal of Geophysical Research: Solid Earth 92*(B8), 7945–7962.

Hearn Jr, B., J. Donnelly-Nolan, and F. Goff (1995). Geologic map and structure sections of the clear lake volcanics, northern california. Technical report, United States Geological Survey.

Herring, T., R. King, and S. McClusky (2010). Introduction to gamit/globk. Technical report, Massachusetts Institute of Technology, Cambridge, Massachusetts.

Hodgson, S. F. (2000). Twenty-three views of the geysers geothermal field, what was said. *Proceedings World Geothermal Congress 2000* (1), 615–619.

Hodgson, S. F. (2010). *A Geysers album: five eras of geothermal history* (3 ed.). California Department of Conservation, Division of Oil, Gas, and Geothermal Resources.

Hulen, J. and D. Norton (2000). Wrench-fault tectonics and emplacement at the geysers felsite. *Transactions - Geothermal Resources Council 24*, 289–298.

Isherwood, W. and R. Chapman (1975). Principal facts for gravity stations in the geysers, clear lake region, california: Us geol. *Survey open-file report 75*(106), 15.

Jeanne, P., J. Rutqvist, C. Hartline, J. Garcia, P. F. Dobson, and M. Walters (2014). Reservoir structure and properties from geomechanical modeling and microseismicity analyses associated with an enhanced geothermal system at the geysers, california. *Geothermics 51*, 460–469.

Jeanne, P., J. Rutqvist, D. Vasco, J. Garcia, P. F. Dobson, M. Walters, C. Hartline, and A. Borgia (2014). A 3d hydrogeological and geomechanical model of an enhanced geothermal system at the geysers, california. *Geothermics 51*, 240–252.

Johnson, C. M. and J. R. O'neil (1984). Triple junction magmatism: A geochemical study of neogene volcanic rocks in western california. *Earth and Planetary Science Letters 71*(2), 241–262.

Johnson, C. W., E. J. Totten, and R. Bürgmann (2016). Depth migration of seasonally induced seismicity at the geysers geothermal field. *Geophysical Research Letters 43*(12), 6196–6204.

Jónsson, S., H. Zebker, P. Segall, and F. Amelung (2002). Fault slip distribution of the 1999 m w 7.1 hector mine, california, earthquake, estimated from satellite radar and gps measurements. *Bulletin of the Seismological Society of America 92*(4), 1377–1389.

Kern, H. (1982). Elastic wave velocities and constants of elasticity of rocks at elevated pressures and temperatures. *Physical Properties of Rocks 1*, 99–140.

Lipman, S., C. Strobel, and M. Gulati (1978). Reservoir performance of the geysers field. *Geothermics 7*(2-4), 209–219.

Lockner, D., R. Summers, D. Moore, and J. Byerlee (1982). Laboratory measurements of reservoir rock from the geysers geothermal field, california. In *International Journal of Rock Mechanics and Mining Sciences & Geomechanics Abstracts*, Volume 19, pp. 65–80. Elsevier.

Lofgren, B. E. (1978). Monitoring crustal deformation in the geysers-clear lake geothermal area, california. Technical report, Geological Survey, Sacramento, CA (USA).

Lohman, R. B. and M. Simons (2005). Locations of selected small earthquakes in the zagros mountains. *Geochemistry, Geophysics, Geosystems 6*(3), 1–10.

Majer, E. and T. McEvilly (1979). Seismological investigations at the geysers geothermal field. *Geophysics 44*(2), 246–269.

Massonnet, D., T. Holzer, and H. Vadon (1997). Land subsidence caused by the east mesa geothermal field, california, observed using sar interferometry. *Geophysical research letters 24*(8), 901–904.

McLaughlin, R. J. (1981). Tectonic setting of pre-tertiary rocks and its relation to geothermal resources in the geysers-clear lake area. *US Geol. Surv. Prof. Pap 1141*, 3–23.

McLaughlin, R. J. and H. N. Ohlin (1984). Tectonostratigraphic framework of the geysers-clear lake region, california. *Franciscan Geology of Northern California* (43), 221–254.

Mogi, K. (1958). Relations between the eruptions of various volcanoes and the deformations of the ground surfaces around them. *Earthq Res Inst 36*, 99–134.

Moore, J., J. Hulen, and D. Norman (1995). Evolution of the geysers (us)-data from fluid-inclusion microthermometry and gas geochemistry. Technical report, Earth Sciences and Resource Institute, Salt Lake City, Utah, USA; New Mexico .

Mossop, A., M. Murray, S. Owen, and P. Segall (1997). Subsidence at the geysers geothermal field: results and simple models. In *Proc. 22nd Workshop on Geothermal Reservoir Engineering, Stanford University, Ca*, Volume 377, pp. 27–29.

Mossop, A. and P. Segall (1997). Subsidence at the geysers geothermal field, n. california from a comparison of gps and leveling surveys. *Geophysical Research Letters 24*(14), 1839–1842.

Mossop, A. and P. Segall (1999). Volume strain within the geysers geothermal field. *Journal of Geophysical Research: Solid Earth 104*(B12), 29113–29131.

O'Connell, D. R. and L. R. Johnson (1991). Progressive inversion for hypocenters and p wave and s wave velocity structure: Application to the geysers, california, geothermal field. *Journal of Geophysical Research: Solid Earth 96*(B4), 6223–6236.

Okada, Y. (1985). Surface deformation due to shear and tensile faults in a half-space. *Bulletin of the seismological society of America 75*(4), 1135–1154.

Oppliger, G., M. Coolbaugh, L. Shevenell, and J. Taranik (2005). Elucidating deep reservoir geometry and lateral outflow through 3-d elastostatic modeling of satellite radar (insar) observed surface deformations: an example from the bradys geothermal field. *Geothermal Resources Council Transactions 29*, 419–424.

Phillips, S., J. Fair, F. I. Henderson, and S. Schwartz (1975, 9). Review of geothermal subsidence. Technical report, University of California, Berkeley and Lawrence Berkeley National Laboratory.

Pritchard, M. E. (2006). Insar, a tool for measuring earth's surface deformation. *Physics Today 59*(7), 68.

Rosen, P. A., E. Gurrola, G. F. Sacco, and H. Zebker (2012). The insar scientific computing environment. In *EUSAR 2012; 9th European Conference on Synthetic Aperture Radar*, pp. 730–733. VDE.

Rutqvist, J. (2011). Status of the tough-flac simulator and recent applications related to coupled fluid flow and crustal deformations. *Computers & Geosciences 37*(6), 739–750.

Rutqvist, J., P. F. Dobson, J. Garcia, C. Hartline, P. Jeanne, C. M. Oldenburg, D. W. Vasco, and M. Walters (2015). The northwest geysers egs demonstration project, california: Pre-stimulation modeling and interpretation of the stimulation. *Mathematical Geosciences 47*(1), 3–29.

Rutqvist, J., P. F. Dobson, C. M. Oldenburg, J. Garcia, and M. Walters (2010). The northwest geysers egs demonstration project phase 1: pre-stimulation coupled geomechanical modeling to guide stimulation and monitoring plans. Technical report, Lawrence Berkeley National Lab.(LBNL), Berkeley, CA (United States).

Rutqvist, J., Y.-S. Wu, C.-F. Tsang, and G. Bodvarsson (2002). A modeling approach for analysis of coupled multiphase fluid flow, heat transfer, and deformation in fractured porous rock. *International Journal of Rock Mechanics and Mining Sciences 39*(4), 429–442.

Sanyal, S. K. and S. L. Enedy (2011). Fifty years of power generation at the geysers geothermal field, california–the lessons learned. In *36th workshop on geothermal reservoir engineering, Stanford, California*.

Schmitt, A. K., M. Grove, T. M. Harrison, O. Lovera, J. Hulen, and M. Walters (2003). The geysers-cobb mountain magma system, california (part 1): U-pb zircon ages of volcanic rocks, conditions of zircon crystallization and magma residence times. *Geochimica et Cosmochimica Acta 67*(18), 3423–3442.

Stanley, W. D., H. M. Benz, M. A. Walters, A. Villaseñor, and B. D. Rodriguez (1998). Tectonic controls on magmatism in the geysers–clear lake region: Evidence from new geophysical models. *Geological Society of America Bulletin 110*(9), 1193–1207.

Stanley, W. D. and R. J. Blakely (1995). The geysers-clear lake geothermal area, californiaan updated geophysical perspective of heat sources. *Geothermics 24*(2), 187–221.

Stark, M. (2003). Seismic evidence for a long-lived enhanced geothermal system (egs) in the northern geysers reservoir. *Transactions-Geothermal Resources Council 23*, 727–732.

Steketee, J. (1958). On volterra's dislocations in a semi-infinite elastic medium. *Canadian Journal of Physics 36*(2), 192–205.

Thomas, R. P., R. H. Chapman, and H. Dykstra (1981). Reservoir assessment of the geysers geothermal field. Technical report, California Div. of Oil and Gas, Sacramento (USA).

Tregoning, P. and C. Watson (2009). Atmospheric effects and spurious signals in gps analyses. *Journal of Geophysical Research: Solid Earth 114*(B9), 1–15.

Tregoning, P. and C. Watson (2011). Correction to atmospheric effects and spurious signals in gps analyses. *Journal of Geophysical Research: Solid Earth 116*(B2), 1–2.

Trugman, D. T., P. M. Shearer, A. A. Borsa, and Y. Fialko (2016). A comparison of long-term changes in seismicity at the geysers, salton sea, and coso geothermal fields. *Journal of Geophysical Research: Solid Earth 121*(1), 225–247.

Vasco, D., J. Rutqvist, A. Ferretti, A. Rucci, F. Bellotti, P. Dobson, C. Oldenburg, J. Garcia, M. Walters, and C. Hartline (2013). Monitoring deformation at the geysers geothermal field, california using c-band and x-band interferometric synthetic aperture radar. *Geophysical Research Letters 40*(11), 2567–2572.

Wdowinski, S., Y. Bock, J. Zhang, P. Fang, and J. Genrich (1997). Southern california permanent gps geodetic array: Spatial filtering of daily positions for estimating coseismic and postseismic displacements induced by the 1992 landers earthquake. *Journal of Geophysical Research: Solid Earth 102*(B8), 18057–18070.

Wright, T., B. Parsons, J. Jackson, M. Haynes, E. Fielding, P. England, and P. Clarke (1999). Source parameters of the 1 october 1995 dinar (turkey) earthquake from sar interferometry and seismic bodywave modelling. *Earth and Planetary Science Letters 172*(1-2), 23–37.